Journal of Computational Physics **177,** 1–36 (2002)
doi:10.1006/jcph.2001.6987, available online at http://www.idealibrary.com on IDEAL®

Time-Dependent Numerical Method with Boundary-Conforming Curvilinear Coordinates Applied to Wave Interactions with Prototypical Antennas

Vianey Villamizar*,[1] and Otilio Rojas†

*Department of Mathematics, Brigham Young University, Provo, Utah 84602; and †Escuela de Computación, Facultad de Ciencias, Universidad Central de Venezuela, Caracas, Venezuela
E-mail: vianey@math.byu.edu, orojas@blues.ciens.ucv.ve

Received January 26, 2001; revised December 7, 2001

A new unstaggered finite-difference time-dependent technique to accurately model scattring from prototypical 2D antenna structures is devised. The unbounded boundary value problems defining these phenomena are redefined over bounded domains using appropriate radiation operators over finite artificial boundaries. Generalized curvilinear coordinates are generated such that physical boundaries correspond to coordinate lines. A numerical procedure to generate almost orthogonal, boundary-conforming, fine grids over these bounded regions is developed. Once the governing equations are written in terms of the new curvilinear coordinates, a time-dependent numerical method is applied to obtain time harmonic steady-state solutions to these problems. The electric field wave amplitude as well as the wave pattern inside the waveguide and the scattered field from the prototypical antennas are obtained. Accuracy and computational cost are compared when almost orthogonal and nonorthogonal grids are in use. An optical theorem for a flanged waveguide antenna with perfect electrical conductor walls is derived. It is verified that the approximate solutions obtained by application of the time-dependent numerical method with boundary-conforming, curvilinear coordinates satisfy the optical theorem.

Key Words: electromagnetic scattering; time-dependent numerical method; orthogonal grid generation; optical theorem.

[1] On leave from Departamento de Matemáticas, Facultad de Ciencias, Universidad Central de Venezuela, Caracas, Venezuela.

0021-9991/02 $35.00

1. INTRODUCTION

Since the pioneering work by Yee [46] numerous works where numerical solutions of electromagnetic scattering problems have been obtained by means of finite-difference techniques have appeared in the electromagnetic literature. Most of them were based on the classical staggered method introduced by Yee and developed and popularized by Taflove and Brodwin [40], which is well known as finite-difference time domain (FDTD). This method and its improved and extended versions have been successfully applied to a great deal of electromagnetic problems. Since Yee's method is based on a uniform cartesian grid, a clear disadvantage of this procedure is that curved electromagnetic structures are staircase approximated, introducing additional errors in the approximation [4, 16, 38]. Two different approaches have evolved to improve the staircasing approximation of curved boundaries and to reduce the errors associated with it. One of them consists in a modification of the cells only in the vicinity of the boundaries while a cartesian grid is maintained in the remainder of the computational domain [5, 6, 14, 19, 30, 33]. These models have been called locally conformal grids and also contour-path finite-difference time domains. They are based on implementation of Ampere and Faraday's laws in integral form at selected cells immediately adjacent to the boundaries whose contours are deformed to conform with surface curvatures. It has been found that some of the methods within this category exhibit late time instability independent of the time step [29].

The second approach consists in a formulation based on global curvilinear coordinates to avoid the staircased approximation. The pioneering work in this direction is due to Holland [15]. Subsequent work was reported by Fusco and Lee *et al*. [8, 9, 25]. The original Cartesian grid is replaced by a convenient global curvilinear grid that fits the boundary. Then Maxwell's equations are written in terms of the new curvilinear coordinates. This results in equations combining the covariant and contravariant components of the electric and magnetic fields, adding to the complexity of the computation. Finally, the staggered FDTD numerical scheme is applied to the new Maxwell's equations over the curvilinear non-cartesian cells. As pointed out in [17], loss of accuracy may result due to the fact that the cell center of the primary grid does not coincide with the edge center of any edge of the dual grid. In [17, 26, 27, 31, 39] unstaggered schemes based on global curvilinear coordinates are presented. In the first of these papers, central difference discretization for spatial derivatives involved in Maxwell's equations is replaced by a combination of forward and backward differencing. In [31, 39] Maxwell's equations are written in conservation form, a global coordinate transformation is implemented, and the Lax–Wendroff upwind scheme is applied to Maxwell's equations in conservation form in terms of the new curvilinear coordinates. This technique is known as finite volume time domain. In [26, 27] the new curvilinear coordinates are obtained numerically by means of a well-known nonorthogonal elliptic grid generator [42]. All of the above works consider structured grids. Unstructured grids have also been considered to model scattering from arbitrarily-shaped domains [10, 11, 29]. They have been called generalized Yee methods. For a detailed account of these methods the reader is referred to [41]. At present, the two approaches continue their development. As recently stated in [41], "the best choice of computational algorithm and mesh remains unclear."

Here, we describe a new finite-difference time-dependent method for the numerical modeling of scattering from 2D prototypical antennas as shown in Fig. 1. We have chosen antennas with different flare angles to show the applicability of the method to arbitrarily-shaped domains. The 90° flare angle antenna will be called flanged waveguide antenna (FWA). The

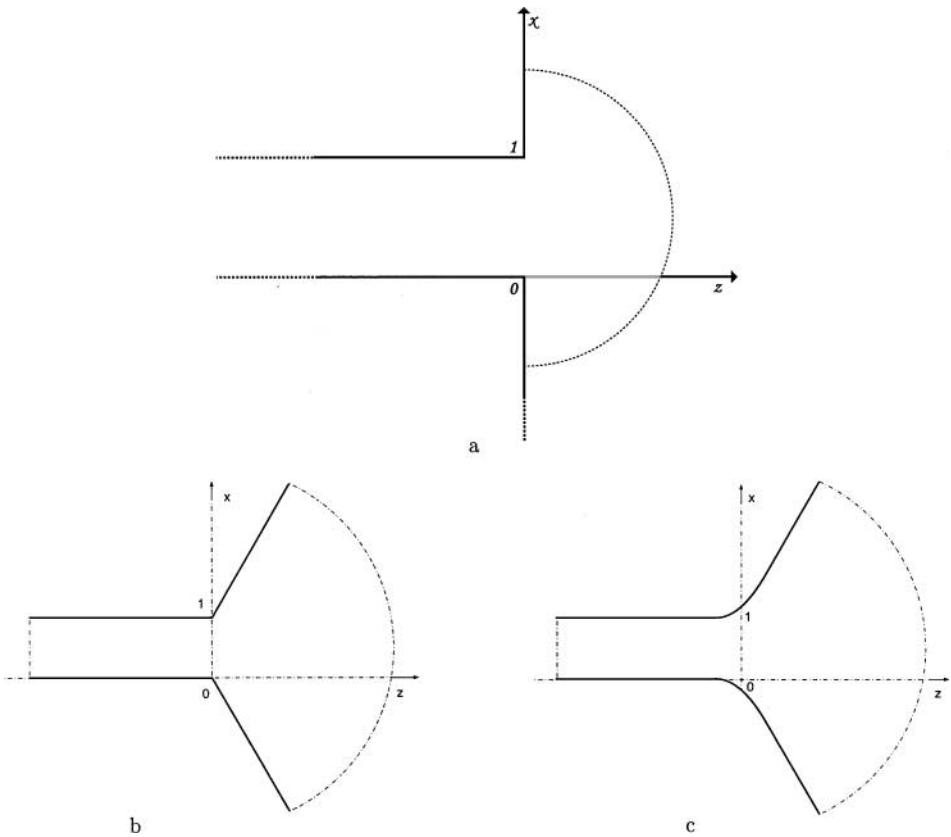

FIG. 1. Prototypical antenna domains.

horn antenna with a smooth bend at the aperture will be called a curved horn antenna (CHA) and the one with nonsmooth bend at the aperture will be called a bent horn antenna (BHA).

We studied the transverse magnetic polarization problem $\mathbf{TM_y}$, but instead of working directly on the system of Maxwell's equations as in all previously-cited work, we reduce Maxwell's equations to a scalar 2D wave equation for the only nonzero component of the electric field. Previous analogous work in 2D electromagnetic scattering modeled by a scalar wave equation only involved Cartesian or cylindrical coordinates [22, 28, 37, 44]. The method is formulated for the flanged waveguide antenna since it can easily be extended to the horn antennas. Before a description of our finite-difference technique is attempted, the original infinite domain needs to be transformed into a finite domain. We define a finite flanged waveguide domain as the bounded region $\mathcal{D}$ enclosed by the open rectangle $-z_\infty \le z < 0$, $0 \le x \le 1$, and the semicircle $0 \le r = (x-1/2)^2 + z^2 \le r_\infty^2$, with $z \ge 0$, where $z = -z_\infty$ and $r = r_\infty$ are fictitious infinite boundaries. This region is illustrated in Fig. 2. To avoid spurious reflections at the fictitious boundaries and the resulting lack of accuracy in the computation, we impose absorbing radiation boundary conditions at the fictitious infinite boundaries. We define these radiation conditions from local annihilating operators acting over asymptotic expansions of the solutions in the far field [1, 2, 13] and at the end of the waveguide [23].

Even for this simplified prototypical antenna, application of the FDTD method will require a special treatment at the fictitious infinite curved boundary at r_∞. Our technique fit

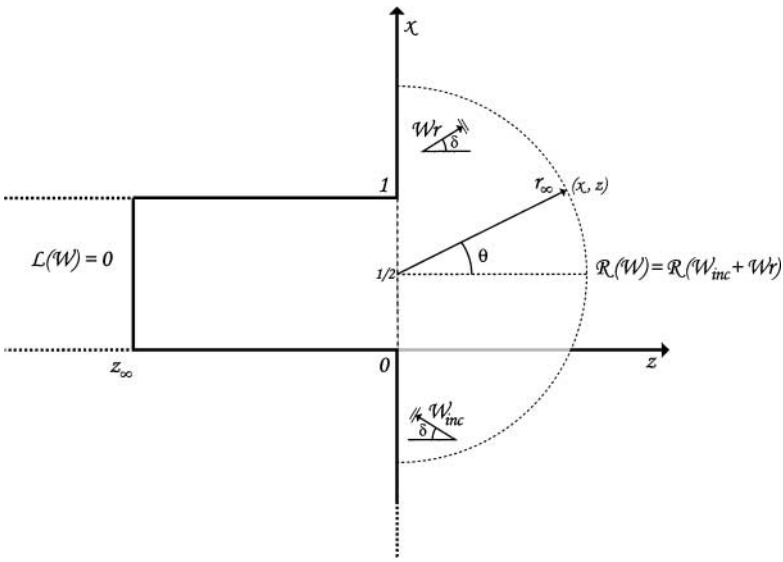

FIG. 2. Receiving problem.

well under the second approach outlined above. We numerically generate various boundary-conforming grids over the antenna domains. Then, we express the governing equations in terms of the new curvilinear coordinates. The space and time derivatives are approximated by central finite difference, and finally by applying an explicit marching in time finite-difference scheme, accurate approximations of the electric field amplitude are obtained. We call this method time dependent with boundary-conforming coordinates or simply TD-BCC. A unique feature of our procedure is the use of second-order local radiation boundary conditions at the end of the waveguide z_∞, and also at r_∞, in terms of curvilinear coordinates.

During the past 10 years FDTD methods have been successfuly applied to model transmitting and receiving antennas of various types and complexities [20, 34, 43]. A more extensive set of references can be found in [41]. Most of these works use staircase or contour-path techniques to approximate the antenna contour, and the fictitious infinite boundaries. Although our computation models very simplified antenna structures, we show through these simple models the potential advantage of using globally conforming boundary techniques combined with numerical grid generation of various types to model scattering from more realistic antennas or complex structures.

A major goal in this work was to determine the influence of grid orthogonality on the accuracy of the numerical approximation and computational cost of the procedure. To the best of our knowledge this is the first time that globally orthogonal grids other than cartesian grids have been used to numerically model scattering of electromagnetic waves from arbitrarily shaped domains. Through numerical validation, we also estabished a relationship between time step and grid size to guarantee numerical stability for TD-BCC method. All of our numerical experiments were found to be free of late time instability, which has been frequently found in other FDTD algorithms. Numerical experiments were performed, changing the incident angle of the incoming wave and the frequency of the incident wave. These experiments allowed us to determine the wave pattern inside and outside the waveguide as a function of the incident angle and frequency.

Based on a conservation of power law and following a recent work by Kriegsmann [24], we derived an optical theorem for a flanged waveguide antenna with perfect electrical

conductor walls. This theorem establishes a relationship among the scattering cross section, transmission coefficients of the solution inside the waveguide, and the leading-order term of the far field amplitude in the direction of the incident wave. Then, we verified that our approximate solutions obtained by application of the TD-BCC satisfy the optical theorem.

2. STATEMENT OF THE WAVE PROPAGATION PROBLEMS

Our prototypical antennas consist of semiinfinite parallel-plate waveguides and the antenna walls extending from the aperture. We assume transverse magnetic polarization with respect to the y-axis, $\mathbf{TM_y}$. Cross sections perpendicular to the y-axis for the flanged waveguide and horn antennas are shown in Fig. 1. The independent variables x and z have been scaled with respect to the guide's width a. We consider an E-polarized plane wave propagating in a plane perpendicular to the y-axis,

$$\mathbf{E^i}(z, x, t) = e^{ik(-\cos(\delta)z+\sin(\delta)x)}\ e^{-ikt}\mathbf{j} = W_{inc}(z, x, t)\mathbf{j}, \tag{1}$$

where δ is the incident angle of the incoming plane wave with the negative z-axis, and k denotes the scaled wave number and frequency, assuming wave speed $c = 1$. Because of the geometry of the domains and the nature of the incident wave, the scattered field and the total electric field $\mathbf{E}(z, x, t)$ are also E-polarized waves in the y direction. Therefore, $\mathbf{E}(z, x, t) = W(z, x, t,)\mathbf{j}$, and the vector Maxwell equation for the electric field reduces to a scalar wave equation for its only nonzero component $W(z, x, t)$ in the y direction,

$$W_{tt} = (W_{xx} + W_{zz}). \tag{2}$$

We also assume that the antenna walls including the waveguide parallel-plate are made of a perfect electrical conductor (PEC). Consequently,

$$\mathbf{E}(z, x, t) \cdot \mathbf{j} = W(z, x, t)\mathbf{j} \cdot \mathbf{j} = W(z, x, t) = 0, \quad \text{in } \mathcal{L}, \tag{3}$$

where $\mathcal{L}$ is the boundary corresponding to the antenna walls. As stated in the Introduction, before any numerical method is applied, it is necessary to redefine the problem over a bounded domain. From this point on, we specialize the problem formulation and the derivation of the numerical method to the flanged waveguide antenna. The method can be easily adapted to the horn antennas and will be discussed later in this work. We have already defined the finite flanged waveguide domain as our bounded region. Therefore, we also need to impose radiation conditions over the artificial boundaries z_∞ and r_∞ to complete the boundary value problem. Following Kriegsmann, Bayliss, and others [1, 2, 13, 23], we obtain these radiation conditions from local annihilating operators acting over asymptotic expansions of the solutions in the far field. First, the total electric field is decomposed as $W = W_{inc} + W_r + W_{sc}$, where W_{inc} is given by (1), $W_r(x, z, t) = -e^{ik(\cos(\delta)z+sen(\delta)x)}e^{-ikt}$ is the specularly reflected wave of W_{inc} from a PEC wall, and W_{sc} is the scattered wave. According to [3], an asymptotic expansion of the scattered field is given by

$$W_{sc}(r, \theta, t) = \frac{e^{ikr}}{\sqrt{r}} \sum_{j=0}^{\infty} \frac{A_j(\theta)}{r^j} e^{-ikt}, \quad r \to \infty, \quad t \to \infty, \tag{4}$$

where $r = (x - 1/2)^2 + z^2$ and $\tan(\theta) = (x - 1/2/z)$. Second, Kriegsmann and Bayliss radiation type operators for applied over (4). As a result, we obtain the radiation conditions

$$R(W)_{r=r_\infty} = R(W_{inc} + W_r + W_{sc})_{r=r_\infty} = R(W_{inc} + W_r)_{r=r_\infty}, \quad z \geq 0, \tag{5}$$

$$L(W)_{z=z_\infty} = 0, \tag{6}$$

where L and R operators are defined as

$$R(W) = W_t + W_r + \frac{W}{2r} \tag{7}$$

$$L(W) = -\sigma \int_0^t \frac{\partial^2 W}{\partial x^2}(z, x, t')\, dt' - \frac{\partial W}{\partial z} + \epsilon \frac{\partial W}{\partial t}. \tag{8}$$

The parameters σ and ϵ were given in (23) as

$$\sigma = \frac{k}{k_1 + k_2}, \quad \epsilon = \frac{k^2 + k_1 k_2}{k(k_1 + k_2)},$$

where $k_n = \sqrt{k^2 - (n\pi)^2}$ for $n = 1, 2 \ldots$.

To finish our boundary value problem, initial conditions need to be included in the formulation. The limiting amplitude principle estabishes that upon excitation of the electromagnetic medium by a time-harmonic force of frequency k the total electric field will also evolve to a time-harmonic steady state of the same frequency regardless of the initial conditions. Therefore, arbitrary initial conditions may be used. For simplicity, we impose null initial conditions in our problems

$$W(z, x, 0) = 0, \quad W_t(z, x, 0) = 0. \tag{9}$$

In brief, Eqs. (1)–(3), (5), (6), and (9) define the receiving boundary value problem for the flanged waveguide antenna, which is illustrated in Fig. 2.

To check the accuracy and computational cost of the numerical method analyzed in this work, we also consider the scattering of an electromagnetic E-polarized plane wave propagating in a plane perpendicular to the y-axis (1), from an infinite PEC wall. A bounded domain for this problem is the fan domain shown in Fig. 3. Boundary conditions over the wall and the artificial boundary $r = r_\infty$ are $W(0, x, t) = 0$ and $R(W) = R(W_{inc} + W_r)$, respectively. Its exact solution can be easily calculated as the superposition of the reflected wave with the incident wave and is given by

$$W(z, x, t) = -2i \sin(kz \cos(\delta)) e^{ikx \sin(\delta)} e^{-ikt}. \tag{10}$$

3. TIME-DEPENDENT NUMERICAL METHOD WITH BOUNDARY-CONFORMING CURVILINEAR COORDINATES

Because of the limiting amplitude principle [32], linear wave propagation problems where a time-harmonic incident wave is present can be modeled either by the Helmholtz equation,

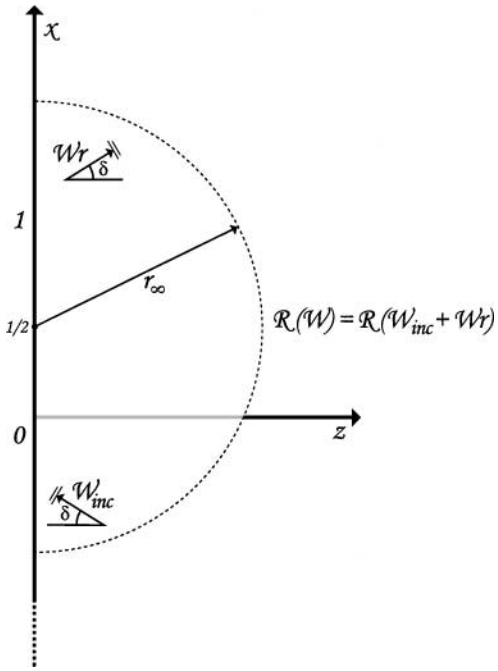

FIG. 3. Scattering from a PEC wall.

also called the frequency-domain equation, or by the corresponding time-dependent wave equation. The solution of the frequency-domain problem can be obtained from the time-dependent problem solution when $t \to \infty$. Time-dependent numerical methods use an explicit finite-difference time marching scheme to obtain the numerical solution of the wave problems. As the time becomes large, the transient state resulting from the initial conditions dies out and the time-dependent solution approaches the harmonic steady-state solution of the corresponding frequency-domain problem. Time-dependent numerical methods have also been applied to scattering problems in acoustics and elasticity [18, 22, 28, 36, 37]. In these areas, there is also a need for numerical methods capable of modeling scattering from obstacles of arbitrary shape.

As mentioned in the Introduction, we use a TD-BCC method to numerically model scattering in the regions shown in Fig. 1. Our approach is rather general; we consider these domains as arbitrary and generate generalized curvilinear coordinate systems such that the boundaries correspond to coordinate lines. These types of coordinates, called boundary-conforming coordinates [21], are generated by an invertible transformation $T : \mathcal{D}' \to \mathcal{D}$, from a rectangular computational domain $\mathcal{D}'$ with coordinates (ξ, η) to the physical domains $\mathcal{D}$ with coordinates (z, x).

More precisely, the transformation is defined as

$$x = x(\xi, \eta) \quad \text{and} \quad y = y(\xi, \eta), \tag{11}$$

where the computational rectangle $\mathcal{D}'$ is formed by all pairs (ξ, η) such that $1 \le \xi \le N_2$ and $1 \le \eta \le N_1$. In Fig. 4, a graphic of this transformation for the bounded flanged waveguide domain is shown. In the process of obtaining a new coordinate system, we also obtain a grid in the physical domain as an image of a rectangular grid in the computational domain.

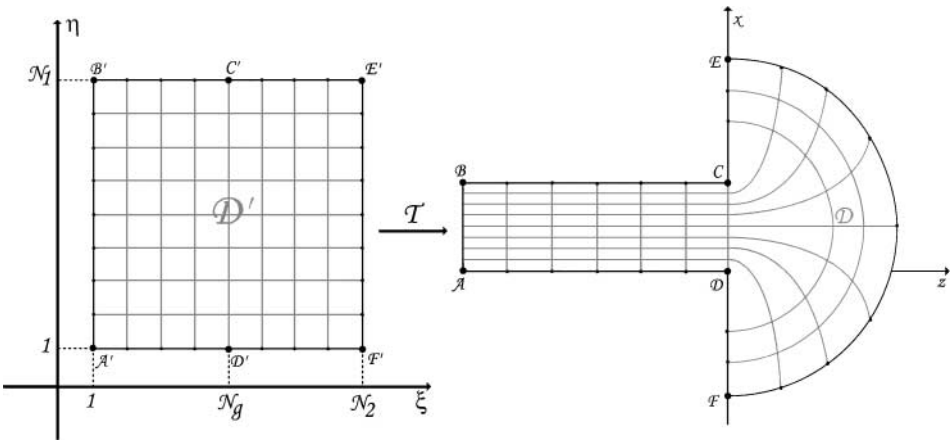

FIG. 4. Transformation from a rectangular domain to a FWA domain.

For simplicity, we choose a rectangular grid in the computational domain $\mathcal{D}'$ with step sizes $\Delta\xi = 1$, $\Delta\eta = 1$, and with N_1 and N_2 nodes in the ξ and η directions, respectively. A finer grid can be generated in the physical domain, keeping the step sizes equal to 1 and increasing the number of nodes N_1 and N_2 of the computational domain. The integer number $\xi = N_g$ corresponds to the number of horizontal nodes in the semiinfinite waveguide. We denote $\xi_i = i * \Delta\xi = i$, $\eta_j = j * \Delta\eta = j$, and the approximations of $x(\xi_i, \eta_j)$ and $z(\xi_i, \eta_j)$ as $x_{i,j}$ and $z_{i,j}$, respectively. To guarantee a smooth transformation, we adopt a differential equation approach to generate the new coordinates (7, 35, 36, 42, 45). First, transformation of the rectangular boundaries into the physical boundaries is defined (see Fig. 4). Then a Dirichlet boundary value problem, defined by a system of partial differential equations in the rectangular region $\mathcal{D}'$, is numerically solved to obtain the transformation from the interior of the rectangular domain to the interior of the physical region. We consider two different systems of partial differential equations and numerically generate three different curvilinear coordinates systems and corresponding grids.

3.1. Boundary Value Problems in Generalized Curvilinear Coordinates

Once the boundary-conforming coordinates have been obtained, the original receiving antenna problems described in Section 2 need to be rewritten in terms of the new coordinates. For instance, the wave equation (2) in generalized curvilinear coordinates ξ and η changes to

$$W_{tt} = J^{-2}(\alpha W_{\xi\xi} - 2\beta W_{\xi\eta} + \gamma W_{\eta\eta}) + J^{-3}(\alpha z_{\xi\xi} - 2\beta z_{\xi\eta} + \gamma z_{\eta\eta})(x_\xi W_\eta - x_\eta W_\xi) + J^{-3}(\alpha x_{\xi\xi} - 2\beta x_{\xi\eta} + \gamma x_{\eta\eta})(z_\eta W_\xi - z_\xi W_\eta), \tag{12}$$

where α, β, and γ are scale metric factors of the transformation T defined by

$$\alpha = x_\eta^2 + y_\eta^2, \quad \beta = x_\xi x_\eta + y_\xi y_\eta, \quad \gamma = x_\xi^2 + y_\xi^2, \tag{13}$$

and J is the determinant or jacobian of the jacobian matrix, $\mathcal{J}$, of the transformation (11). Evidently, Eq. (12), although still linear, is more complex than the original wave equation. The advantage of the transformation is that this equation is defined over a rectangular domain now. Thus, a finite-difference approximation of the derivatives near the boundaries

can be performed without interpolation in the computational independent variables ξ and η. Moreover, under certain conditions on the properties of the transformation, Eq. (12) can be greatly simplified. We will take advantage of this simplification later on this work.

On the other hand, boundary conditions over the antenna walls in terms of ξ and η are written as

$$W(\xi, 1, t) = 0, \quad W(\xi, N_1, t) = 0, \quad 1 \le \xi \le N_2, \quad t > 0, \tag{14}$$

while radiation conditions for these receiving problems are given by

$$L_{\xi\eta}(W)(1, \eta, t) = 0, \tag{15}$$

$$R_{\xi\eta}(W)(N_2, \eta, t) = R_{\xi\eta}(W_{inc} + W_r)(N_2, \eta, t), \quad 1 \le \eta \le N_1, \quad t > 0. \tag{16}$$

The incident wave W_{inc} was defined in (1), and W_r is the corresponding reflected wave. The operators $L_{\xi\eta}$ and $R_{\xi\eta}$ in terms of ξ η are given by

$$L_{\xi\eta}(W) = -\frac{\sigma}{J^2} z_\xi^2 \int_0^t \frac{\partial^2 W}{\partial \eta^2}\, dt' - \frac{1}{J}\left(x_\eta \frac{\partial W}{\partial \xi} - x_\xi \frac{\partial W}{\partial \eta}\right) + \epsilon \frac{\partial W}{\partial t}, \tag{17}$$

$$R_{\xi\eta}(W) = \frac{\partial W}{\partial t} + \frac{\cos(\delta)}{J}\left(x_\eta \frac{\partial W}{\partial \xi} - x_\xi \frac{\partial W}{\partial \eta}\right) + \frac{\sin(\delta)}{J}\left(-z_\eta \frac{\partial W}{\partial \xi} + z_\xi \frac{\partial W}{\partial \eta}\right) + \frac{W}{2\sqrt{x^2(\xi, \eta) + z^2(\xi, \eta)}}. \tag{18}$$

A brief outline of the various grids to be generated in the following three sections will now be given. At first, we will generate boundary-conforming grids over the antenna domain by applying a Winslow or a homogeneous Thompson, Tames, Mastin (TTM) generator [21]. It will be shown that TTM grids are strongly nonorthogonal in our antenna domains. So we will generate almost orthogonal grids in an attempt to improve the accuracy of the numerical method and decrease the computational cost. We will apply Eca and Ryskin–Leal techniques [7, 35] also known as the scaled-Laplacian generator, over the antenna domain. As a result, we will obtain almost orthogonal grids. However, they will not be sufficiently fine to obtain accurate solutions for the FWA domain. The scaled-Laplacian grid generator algorithm will fail to converge for step sizes smaller than certain values at those aperture corner points where the angle between the grid lines is close to 270° for the FWA domain. To avoid this problem, the FWA domain will be divided into two regions: a finite rectangular waveguide from the artificial boundary at $z = z_\infty$ to the aperture at $z = 0$, and the region enclosed by a semicircle of radius r_∞ for $z \ge 0$, which will be called the "fan domain." A uniform rectangular grid will be trivially defined inside the waveguide by means of equally spaced vertical and horizontal lines, while an orthogonal non-Cartesian grid will be obtained using a scaled-Laplacian generator for the fan domain. These two grids will be matched at the aperture using osculating polynomials that we call generalized fifth-order Hermite polynomials. It will be shown that the new grid is orthogonal everywhere except at a few nodes near to the aperture, but more importantly, it will also be shown that this grid can be made as fine as needed for the accuracy of the TD-BCC method.

3.2. Grids Generated Using the TTM Technique

In this section, we show nonorthogonal grids generated from the numerical solution of a Dirichlet boundary value problem defined by an elliptic system of partial differential equations given by

$$\begin{aligned} \alpha z_{\xi\xi} - 2\beta z_{\xi\eta} + \gamma z_{\eta\eta} &= 0, \\ \alpha x_{\xi\xi} - 2\beta x_{\xi\eta} + \gamma x_{\eta\eta} &= 0, \end{aligned} \tag{19}$$

with α, β, and γ defined as in (13). This method is known as the Winslow or homogeneous TTM grid generator [21]. It is very easy to implement and usually produces unfolded grids. The starting point for this method, as well as for the others to be described later, is to choose points over the rectangular boundaries and assign them to boundary points over the mushroom domain. This constitutes a Dirichlet boundary condition. In our case, we assign all the N_1 nodes in the vertical segment $A'B'$ in $\mathcal{D}'$ to corresponding nodes over the vertical segment AB in $\mathcal{D}$. The other boundary segments of the rectangular computational domain D' are likewise assigned as is shown in Fig. 4. Once the generator system of partial differential equations is discretized, a successive overrelaxation method (SOR) is employed to produce the new nodes in the physical domain. In Fig. 5, a grid generated according to this method is illustrated for the data $z_\infty = 3$, $r_\infty = 3$, $N_1 = 51$, $N_2 = 70$, $N_g = 30$, $\omega = 1.85$, and $\text{tol} = 10^{-4}$, where ω is a relaxation parameter and tol in the maximum difference allowed between two successive approximations at every node.

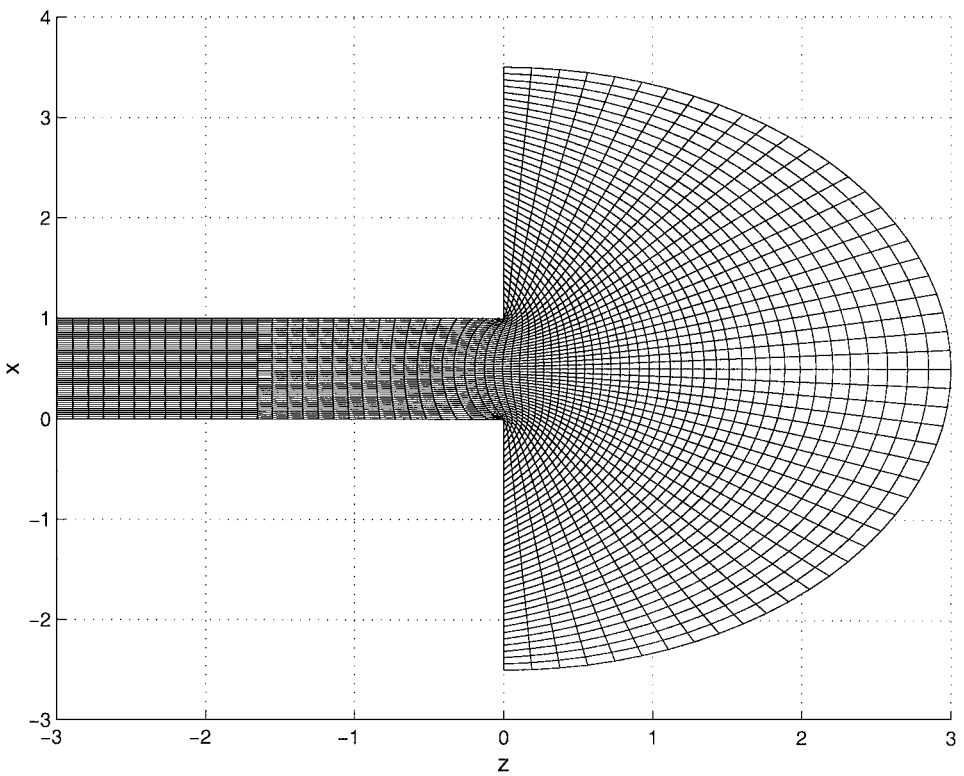

FIG. 5. Grid for FWA domain generated by TTM algorithm.

TABLE I
TTM Grids Experiments in the FWA Domain

r_∞/z_∞	$N_1 \times N_2$ (N_g)	$J_{\min}$; (z, x)	MDO; (z, x)	ADO	Iters
3/3	51×70 (30)	5×10^{-4}; $(-0.03, 0.98)$	74.8; $(-0.03, 0.98)$	11.1	150
3/3	70×70 (30)	2.7×10^{-4}; $(-0.02, 1)$	78.9; $(-0.02, 0.01)$	11.2	236
3/3	100×120 (50)	8.2×10^{-5}; $(-0.02, 1)$	82.7; $(-0.02, 0.01)$	11.6	444
3/3	130×150 (50)	5.6×10^{-5}; $(-0.02, 1)$	85.7; $(-0.02, 1)$	13.6	709
6/5	180×220 (90)	8.8×10^{-6}; $(-0.01, 1)$	88.6; $(-0.01, 1)$	11.9	1250

Grid orthogonality is an important property in grid generation. We are adopting some grid orthogonality parameters introduced in [7]. For instance, the maximum and mean deviation from orthogonality, MDO and ADO, respectively, are defined as

$$\begin{aligned} \text{MDO} &= \text{Max}|90^\circ - \theta_{i,j}|, \quad 2 \le i \le N_2 - 1; \quad 2 \le j \le N_1 - 1 \\ \text{ADO} &= \left(\frac{1}{N_1 - 2}\right)\left(\frac{1}{N_2 - 2}\right) \sum_{i=2}^{N_2-1} \sum_{j=2}^{N_1-1} (|90^\circ - \theta_{i,j}|). \end{aligned} \tag{20}$$

Here, the angle $\theta_{i,j}$ is a discrete approximation for the local distortion angle between grid lines at the point $(z_{i,j},\ x_{i,j})$,

$$\theta_{i,j} = \arccos\left(\frac{\beta_{i,j}}{\alpha_{i,j}\gamma_{i,j}}\right).$$

A summary of the characteristics of different grids resulting from the application of the TTM grid generator to the FWA domain is reported in Table I. The column $J_{\min}$ contains the minimum value of the Jacobian as an indicator of possible singularities. The Iters column reports the number of iterations required for the TTM method to reach convergence. The FWA domain has an abrupt change of 270° at the corner points C and D of the aperture (see Fig. 4). Therefore, neighboring grid lines experience this abrupt change as they go through the aperture. As a consequence, TTM grids are far from being orthogonal at this region as shown in Table I. We also notice that the maximum deviation from orthogonality as well as the number of iterations increases for grid refinement. The values $J_{\min}$ and MDO were reached at the aperture, where the abrupt change is present. The relaxation parameter ω and the tolerance, tol, were kept fixed at 1.85 and 10^{-4}, respectively, for all the experiments reported in Table I. TTM grid generator proved to be very reliable for this domain. In fact, we were able to generate very fine grids at low computational cost, as can be seen in Table I.

In Section 2, we described the scattering of a plane electromagnetic wave from a PEC wall. The time-domain numerical method combined with grid generation techniques will also be applied to this benchmark problem. Thus, grids need to be generated for this domain, which we have called the fan domain. The coordinate transformation is illustrated in Fig. 6. The rectangular boundaries are assigned in a way that resembles the assignment for the FWA domain without the waveguide. The grid shown in Fig. 7 was generated by applying the TTM grid generator method with the following data: $r_\infty = 3$, $N_1 = 100$, $N_2 = 60$, $\omega = 1.85$, and $\text{tol} = 10^{-4}$.

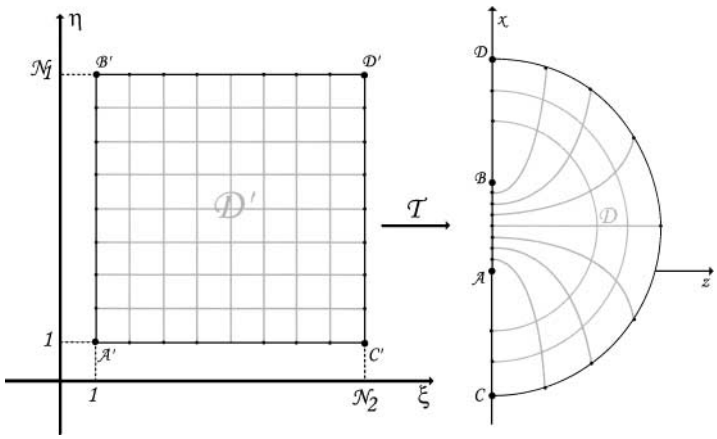

FIG. 6. Transformation from a rectangular domain to a fan domain.

In Table II, properties of various fan domain grids obtained by application of the TTM grid generator are recorded. They show a strong departure from orthogonality at the left boundary, which corresponds to the aperture in the FWA domain.

However, MDO is smaller for this case, as is expected, since the maximum angle between grid lines for the fan domain is below 180°. As in Table I, the relaxation parameter ω and the tolerance, tol, were kept fixed at 1.85 and 10^{-4}, respectively, for all the reported experiments.

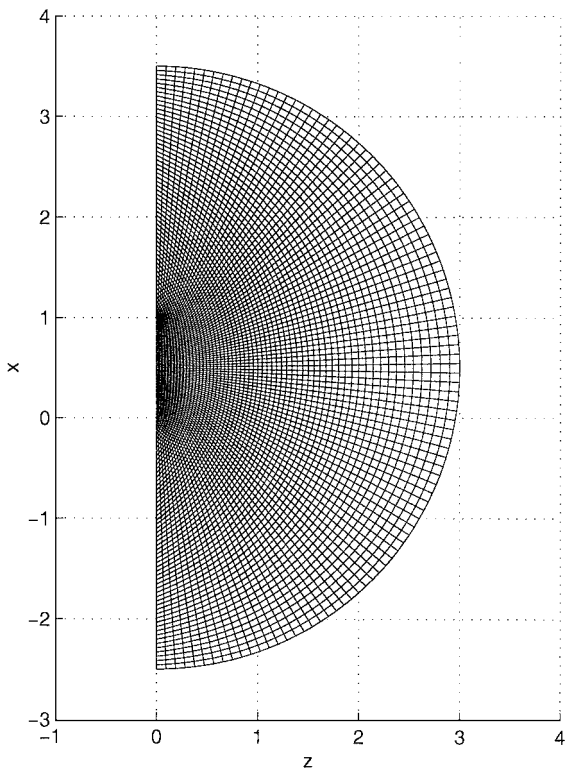

FIG. 7. Fan grid generated by TTM algorithm.

TABLE II
TTM Grid Experiments in the Fan Domain

r_∞	$N_1 \times N_2$	$J_{\min}$; (z, x)	MDO; (z, x)	ADO	Iters
3	51×40	3.9×10^{-4}; (0, 1)	66.1; (0, 0.02)	21.9	74
3	70×40	2.3×10^{-4}; (0, 1)	71.6; (0, 0.01)	22.2	112
3	100×60	10^{-4}; (0, 1)	72.7; (0, 0.01)	21.9	220
3	130×100	5×10^{-5}; (0, 1)	71.1; (0, 0.01)	21.6	401
6	180×130	3.5×10^{-5}; (0, 1)	79.4; (0, 0.01)	22	812

3.3. Almost Orthogonal Grids Generated Using Scaled-Laplacian Equations

Orthogonal grids are identified as those for which the parameter $\beta = x_\xi x_\eta + y_\xi y_\eta$ of the coordinates transformation T is null. It is well known [7, 35] that the orthogonal coordinates $z(\xi, \eta)$, y $x(\xi, \eta)$ are solutions of the nonlinear system of differential equations

$$\begin{aligned} \frac{\partial}{\partial \xi}\left(f\frac{\partial z}{\partial \xi}\right) + \frac{\partial}{\partial \eta}\left(\frac{1}{f}\frac{\partial z}{\partial \eta}\right) = 0, \\ \frac{\partial}{\partial \xi}\left(f\frac{\partial x}{\partial \xi}\right) + \frac{\partial}{\partial \eta}\left(\frac{1}{f}\frac{\partial x}{\partial \eta}\right) = 0, \end{aligned} \tag{21}$$

where the function $f(\xi, \eta)$ is known as a distortion function and is defined by

$$f(\xi, \eta) = \frac{\left(z_\eta^2 + x_\eta^2\right)^{1/2}}{\left(z_\xi^2 + x_\xi^2\right)^{1/2}}. \tag{22}$$

System (21), widely used in orthogonal grid generation, is known as scaled-Laplacian. We define an orthogonal grid generation method that consists of imposing boundary conditions over the physical domain boundary and numerically solving a Dirichlet boundary value problem by iterative methods. We assume that $f(\xi, \eta)$ is known from the previous iteration step, linearizing the original system. Two cycles are involved in the iteration process. One is performed until the distortion function f has been approximated within a reasonable tolerance (global cycle). The second is the inner cycle necessary for approximating the coordinate values for each fixed value of f. Our approach is similar to Eca's approach [7], but instead of discretizing the original system (21), we perform the derivatives first and then discretize the resulting equation. The advantage is that we do not need to evaluate f between nodes, as in Eca's work. In fact,

$$\begin{aligned} f_{i,j} &= \left[\frac{(z_{i,j+1} - z_{i,j-1})^2 + (x_{i,j+1} - x_{i,j-1})^2}{(z_{i+1,j} - z_{i-1,j})^2 + (x_{i+1,j} - x_{i-1,j})^2}\right]^{1/2} \\ f_{1,j} &= \left[\frac{(z_{1,j+1} - z_{1,j-1})^2 + (x_{1,j+1} - x_{1,j-1})^2}{(-3z_{1,j} + 4z_{2,j} - z_{3,j})^2 + (-3x_{1,j} + 4x_{2,j} - x_{3,j})^2}\right]^{1/2} \\ f_{N_2,j} &= \left[\frac{(z_{N_2,j+1} - z_{N_2,j-1})^2 + (x_{N_2,j+1} - x_{N_2,j-1})^2}{(3z_{N_2,j} - 4z_{N_2-1,j} + z_{N_2-2,j})^2 + (3x_{N_2,j} - 4x_{N_2-1,j} + x_{N_2-2,j})^2}\right]^{1/2} \\ f_{i,1} &= \left[\frac{(-3z_{i,1} + 4z_{i,2} - z_{i,3})^2 + (-3x_{i,1} + 4x_{i,2} - x_{i,3})^2}{(z_{i+1,1} - z_{i-1,1})^2 + (x_{i+1,1} - x_{i-1,1})^2}\right]^{1/2}, \\ f_{i,N_1} &= \left[\frac{(3z_{i,N_1} - 4z_{i,N_1-1} + z_{i,N_1-2})^2 + (3x_{i,N_1} - 4x_{i,N_1-1} + x_{i,N_1-2})^2}{(z_{i+1,1} - z_{i-1,1})^2 + (x_{i+1,1} - x_{i-1,1})^2}\right]^{1/2}, \end{aligned} \tag{23}$$

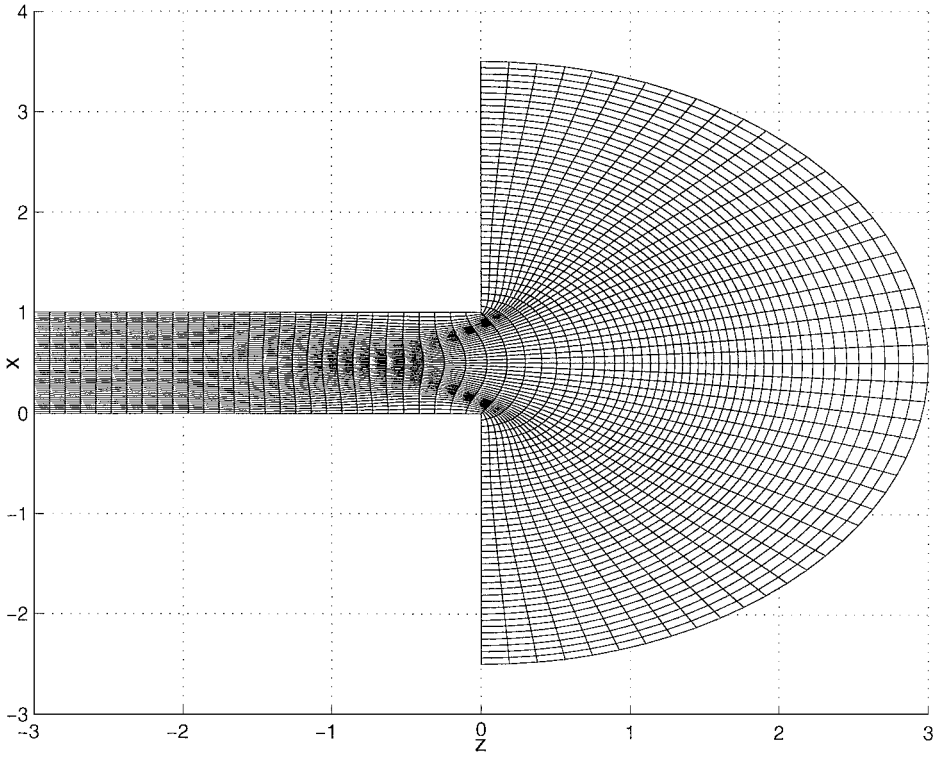

FIG. 8. OG grid for FWA domain generated by scaled-Laplacian algorithm.

for $j = 2, \ldots, N_1 - 1$ and $i = 2, \ldots, N_2 - 1$. In Figs. 8 and 9, grids generated using this method are shown. We will call them simply OG grids. In Fig. 8 we used as data $z_\infty = 3$, $r_\infty = 3$, $N_1 = 51$, $N_2 = 70$, $N_g = 30$, $\omega = 1.85$, Globaltol $= 5 \times 10^{-3}$, and Innertol $= 10^{-4}$. Likewise in Fig. 9, the following data were used, $r_\infty = 3$, $N_1 = 100$, $N_2 = 60$, $\omega = 1.85$, Globaltol $= 5 \times 10^{-3}$, and Innertol $= 10^{-4}$. The grid orthogonality tendency in these figures is clearly evident when they are compared with nonorthogonal TTM grids in Figs. 5 and 7, respectively. The parameter Globaltol represents the tolerance used for the distortion function convergence. Innertol is the tolerance used to stop the SOR inner cycle.

The shadow region in Fig. 8 shows grid line concentration at the middle of the waveguide close to the aperture and at the aperture corners. This undesirable concentration avoids convergence of the orthogonal algorithm for relatively coarse grid consisting of $70 \times 70(30)$ nodes or finer in the FWA domain with $r_\infty/z_\infty = 3/3$. As stated above, computational grids with this many nodes or more are needed for accuracy purposes.

In Tables III and IV the orthogonality property is clearly stated with a maximum orthogonality deviation less than 4° for the fan domain, less than 6° for the FWA, and mean deviation orthogonality less than 0.2° in both cases. The column *GlIts/InIts* corresponds to the ratio of inner cycle and global cycle iterations. The *GlTol* contains the values for the global cycle tolerance. Contrary to what happens in the FWA domain, very fine OG grids can be obtained in the fan domain, as can be seen in Table IV. This fact will be exploited in the next section to construct an algorithm capable of generating almost orthogonal grids sufficiently fine for our computational purposes. It is also observed from J_{min} values that grids generated with this orthogonal algorithm experience less distortion than those generated by the TTM algorithm.

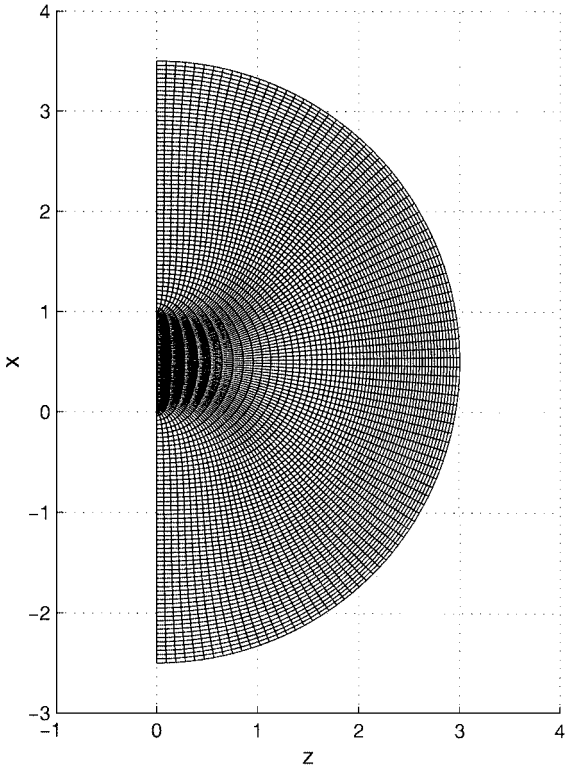

FIG. 9. Fan OG grid generated by scaled-Laplacian algorithm.

3.4. Nearly Orthogonal Grid Generation Using Generalized Hermite Interpolation Matching

An accurate approximation of the boundary value problems solutions analyzed in this work requires finer grids than those already obtained by the orthogonal method described in the above section. In this section, we obtain almost orthogonal fine grids by decomposing the FWA domain in two regions: a finite waveguide (rectangular domain) and a fan domain (semicircular region). A uniform rectangular grid is trivially defined inside the waveguide by means of equally spaced vertical and horizontal lines, while an orthogonal grid is obtained using a scaled-Laplacian generator inside the fan domain as described in Section 3.3. These two domains with their respective grids are brought together and are matched at common aperture nodes using generalized fifth-order Hermite polynomials. The new grid is orthogonal everywhere except at a few nodes near the aperture, but more importantly, this grid is smooth with continuous second-order derivatives and can be made as fine as needed for the accuracy of the TD-BCC method. We call this grid almost orthogonal Hermite grid (OHG).

TABLE III
Orthogonal OG Grid Experiments in the FWA Domain

r_∞/z_∞	$N_1 \times N_2$ (N_g)	$J_{\min}$	MDO; (z, x)	ADO	*GlIts/InIts*	*GlTol*
3/3	40×70 (30)	-1.3×10^{-4}	5.34; (−.1, 1)	0.15	59/894	5×10^{-3}
3/3	51×70 (30)	-1.3×10^{-4}	5.65; (−.1, 1)	0.13	57/937	5×10^{-3}
3/3	60×70 (30)	-1.6×10^{-4}	5.74; (−.1, .0.01)	0.13	130/1023	5×10^{-3}
6/5	70×70 (30)	-5×10^{-4}	5.47; (.02, 1)	0.12	99/1516	5×10^{-3}

TABLE IV
Orthogonal OG Grid Experiments in the Fan Domain

r_∞	$N_1 \times N_2$	$J_{\min}$; (z, x)	MDO; (z, x)	ADO	*InIts*	*GlTol*
3	51×40	-3.6×10^{-3}; (.05, −.05)	2.63; (.12, .96)	0.17	607	10^{-3}
3	100×60	1.2×10^{-3}; (.12, .86)	3.02; (.08, .99)	0.08	1034	5×10^{-4}
3	130×90	-6.5×10^{-4}; (.09, .1)	3.61; (.06, .99)	0.05	2268	2.5×10^{-4}
6	220×140	-4.3×10^{-4}; (0.4, .91)	2.39; (.06, .99)	0.03	1663	2.5×10^{-4}

The matching is performed over the coordinate lines $(z(\xi, \eta_j), x(\xi, \eta_j))$, $j = 2, \ldots, N_1 - 1$, η_j fixed, and $\xi \in [1, N_2]$. We consider only the waveguide points: $(N_g - 2, \eta_j)$, $(N_g - 1, \eta_j)$, and (N_g, η_j). The z coordinate can be parameterized as $z = z(\xi, \eta_j) = (\xi - N_g) * \Delta z$, since $\Delta z = z_\infty/(N_g - 1)$ has been chosen constant in the waveguide. Evidently, $z(\xi, \eta_j)$ has the required smoothness. To guarantee continuous second-order derivatives for the parametric coordinate $x(\xi, \eta_j)$, we construct Hermite fifth-order polynomials $H_j(\xi)$ for each $j = 2, \ldots, N_1 - 1$ to interpolate $x(\xi, \eta_j)$ between the nodes $(N_g - 2, \eta_j)$, $(N_g - 1, \eta_j)$, and (N_g, η_j) that satisfy

$$\begin{aligned} &H_j(N_g - 2) = x(N_g - 2, \eta_j), \\ &\frac{dH_j}{d\xi}(N_g - 2) = \frac{d^2H_j}{d\xi^2}(N_g - 2) = 0, \\ &H_j(N_g) = x\left(N_g^+, \eta_j\right), \\ &\frac{dH_j}{d\xi}(N_g) = (x_\xi)_{N_g^+, \eta_j}, \quad \frac{d^2H_j}{d\xi^2}(N_g, \eta_j) = (x_{\xi\xi})_{N_g^+, \eta_j}. \end{aligned} \tag{24}$$

We have $x(N_g - 2, \eta_j) = (j - 1)/(N_1 - 1)$, since we are using a uniform partition for the left waveguide end vertical segment. Thus the matching Hermite fifth-order polynomials defined for $\xi \in [N_g - 2, N_g]$ are given by

$$\begin{aligned} H_j(\xi) = (j - 1)/(N_1 - 1) &+ \frac{(x_\xi)_{N_g^+, j}}{8}(\xi - N_g + 2)^3(\xi - N_g) \\ &+ \frac{(x_{\xi\xi})_{N_g^+, \eta_j} - 3(x_\xi)_{N_g^+, \eta_j}}{16}(\xi - N_g + 2)^3(\xi - N_g)^2. \end{aligned} \tag{25}$$

Table V contains several grid generation experiments using the OHG generating method. It should be noticed that the orthogonality is lost along the interpolation vertical segments corresponding to the coordinate lines $\xi = N_g - 1$ and $\xi = N_g$ in the computational domain. However, the orthogonality average ADO reveals that these are the only points where a

TABLE V
OHG Grid Experiments in FWA Domain

r_∞/z_∞	$N_1 \times N_2$ (N_g)	$J_{\min}$; (z, x)	MDO; (z, x)	ADO
3/3	51×70 (30)	-1.5×10^{-3}; (0, 0.02)	29; (0, 0.02)	0.17
3/3	71×60 (30)	-1.02×10^{-3}; (0, 0.01)	28.07; (0, 0.01)	0.16
3/3	130×150 (60)	-2.7×10^{-4}; (−.05, .97)	29.2; (0, .007)	0.048
6/5	220×220 (80)	-1.7×10^{-4}; (−0.06, 0.97)	33.3; (0, .005)	0.036

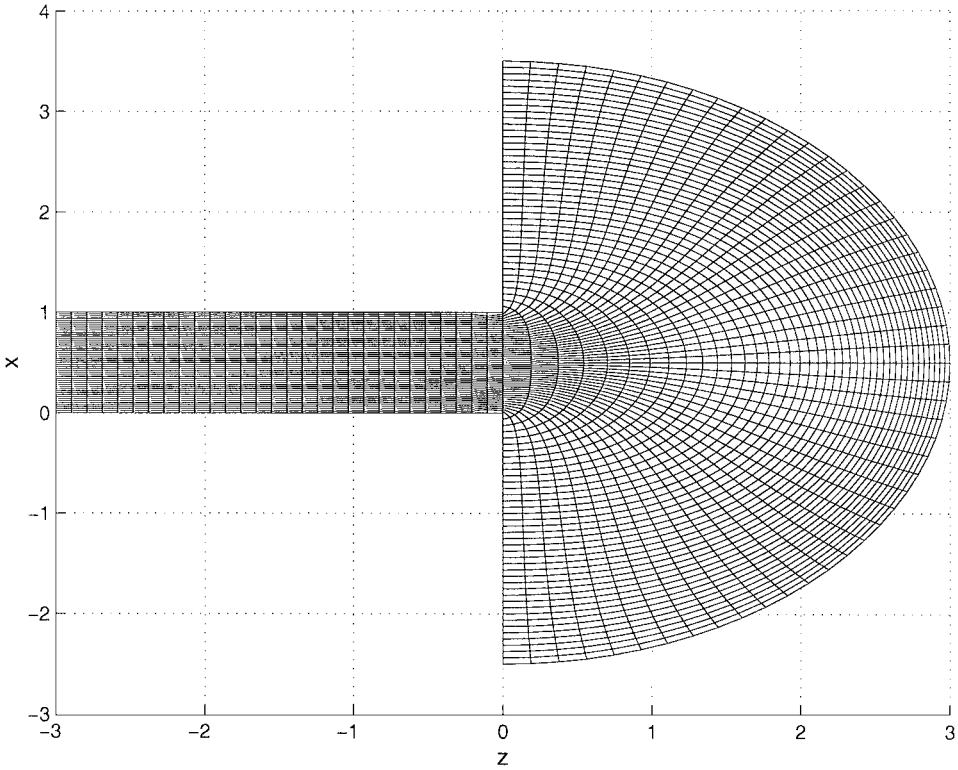

FIG. 10. Almost orthogonal Hermite grid (OHG) for FWA domain.

deviation from orthogonality is observed. An OHG grid is illustrated in Fig. 10 for $r_\infty = 3$, $N_1 = 51$, $N_2 = 70$, and $N_g = 30$.

3.5. Finite-Difference Equations and Numerical Procedures

The numerical scheme is an explicit finite-difference second-order method in both space and time. The domain is the rectangular region $R = \{(\xi, \eta) \in [1, N_2] \times [1, N_1]\}$ in the ξ–η plane. For convenience, spatial step sizes have been chosen as $\Delta\xi = \Delta\eta = 1$. Thus, for a mesh refinement N_1 and N_2 are increased. The temporal step Δt is chosen so that numerical stability is guaranteed. We denote $\xi_i \equiv i\,\Delta\xi = i$, $\eta_j \equiv j\,\Delta\eta = j$, and $t_n = n\,\Delta t$, where $1 \le i \le N_2$, $1 \le j \le N_1$, and $n = 0, \ldots, NT$. The solution of the difference equation at the point (ξ_i, η_j, t_n) is defined as $W^n_{i,j}$.

The wave equation in generalized curvilinear coordinates (12) greatly simplifies in TTM coordinates. In fact, according to coordinate transformation (19), this equation reduces to

$$W_{tt} = \frac{1}{J^2}(\alpha W_{\xi\xi} - 2\beta W_{\xi\eta} + \gamma W_{\eta\eta}). \tag{26}$$

A different simplification occurs for orthogonal grids, since all terms containing β as a factor cancel. Therefore, we use Eq. (12) for general grids, but for TTM or orthogonal grids we use their corresponding simplification. For interior points ($i = 2, \ldots, N_2 - 1$, $j =$

$2, \ldots, N_1 - 1$, and $n = 0, 1, \ldots$), Eq. (26) in differenced form is given by

$$W_{i,j}^{n+1} = 2\left[1 - \left(\frac{\Delta t}{J_{i,j}}\right)^2 (\alpha_{i,j} + \gamma_{i,j})\right] W_{i,j}^n - W_{i,j}^{n-1} + \left(\frac{\Delta t}{J_{i,j}}\right)^2 \alpha_{i,j}\left(W_{i+1,j}^n + W_{i-1,j}^n\right)$$
$$- \left(\frac{\beta_{i,j} J_{i,j}^2}{2\Delta t^2}\right)\left[W_{i+1,j+1}^n - W_{i+1,j-1}^n - W_{i-1,j+1}^n + W_{i-1,j-1}^n\right]$$
$$+ \left(\frac{\Delta t}{J_{i,j}}\right)^2 \gamma_{i,j}\left(W_{i,j+1}^n + W_{i,j-1}^n\right), \tag{27}$$

where $\alpha_{i,j}$, $\beta_{i,j}$, $\gamma_{i,j}$, and $J_{i,j}$ are the metric factors and Jacobian in differenced form. They are defined as

$$\alpha_{i,j} = \frac{1}{4}[(z_{i+1,j} - z_{i-1,j})^2 + (x_{i+1,j} - x_{i-1,j})^2]$$
$$\beta_{i,j} = \frac{1}{4}[(z_{i+1,j} - z_{i-1,j})(z_{i,j+1} - z_{i,j-1}) + (x_{i+1,j} - x_{i-1,j})(x_{i,j+1} - x_{i,j-1})]$$
$$\gamma_{i,j} = \frac{1}{4}[(z_{i,j+1} - z_{i,j-1})^2 + (x_{i,j+1} - x_{i,j-1})^2]$$
$$J_{i,j} = \frac{1}{4}[(z_{i,j+1} - z_{i,j-1})(x_{i+1,j} - x_{i-1,j}) - (z_{i+1,j} - z_{i-1,j})(x_{i,j+1} - x_{i,j-1})].$$

Therefore, a 10-point numerical scheme marching in time is obtained. Similar finite-difference equations with some more terms are obtained for the general equation (12) and the equation corresponding to orthogonal coordinates. In Fig. 11, a graphic description of this scheme is provided. Computation at the fictitious infinite boundaries, $i = 1$ or $i = N_2$, is cumbersome. Therefore, after substitution in the differenced equation (27), evaluation at points out of the rectangular domain occurs. An appropriate combination of the differenced

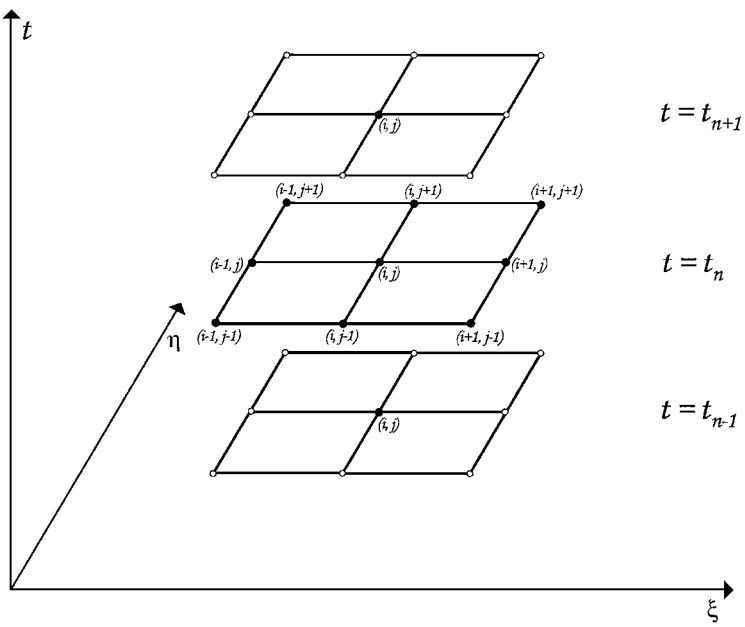

FIG. 11. Time-dependent numerical scheme.

form of the boundary operator $L_{\xi\eta}$ and $R_{\xi\eta}$ with Eq. (27) leads to the approximate values of $W_{1,j}^{n+1}$ and $W_{N_2,j}^{n+1}$. As was stated at the beginning of Section 3, the time harmonic steady state of $W(\xi, \eta, t)$ is reached when $t \to \infty$. We use the following stop criteria to determine numerically this steady state for a given value Tol > 0,

$$\max_{1\le i\le N_2,\ 2\le j\le N_1-1} \left\| W_{i,j}^{n+1} \right| - \left| W_{i,j}^{n} \right\| < \text{Tol}.$$

4. DISCUSSION OF NUMERICAL RESULTS FOR THE FLANGED WAVEGUIDE ANTENNA

In this section, we analyze the numerical results obtained when the TD-BCC method is applied to the receiving antenna problem described in Section 2. We have generated three different types of grids for the FWA and fan domains. Here, we show how the accuracy and computational cost invested in calculating the numerical solution depends on the grid structure. We also perform two types of numerical experiments. One shows the grid refinement effect on the accuracy of the numerical solution. The other experiment establishes the effectiveness of the radiation conditions by changing the fictitious infinite boundary locations.

In Figs. 12 and 13 the amplitudes $|W(z, x, t_\infty)|$ of the total electric field for the receiving antenna problem are shown. They were obtained using OHG grids, an angle of incidence $\delta = 0^\circ$, frequency $k = 3\pi/2$, and a stop criterion tolerance Tol $= 10^{-4}$. Two different sizes for the FWA domain were analyzed. In Fig. 12, the exterior region was modeled with $r_\infty = 3$,

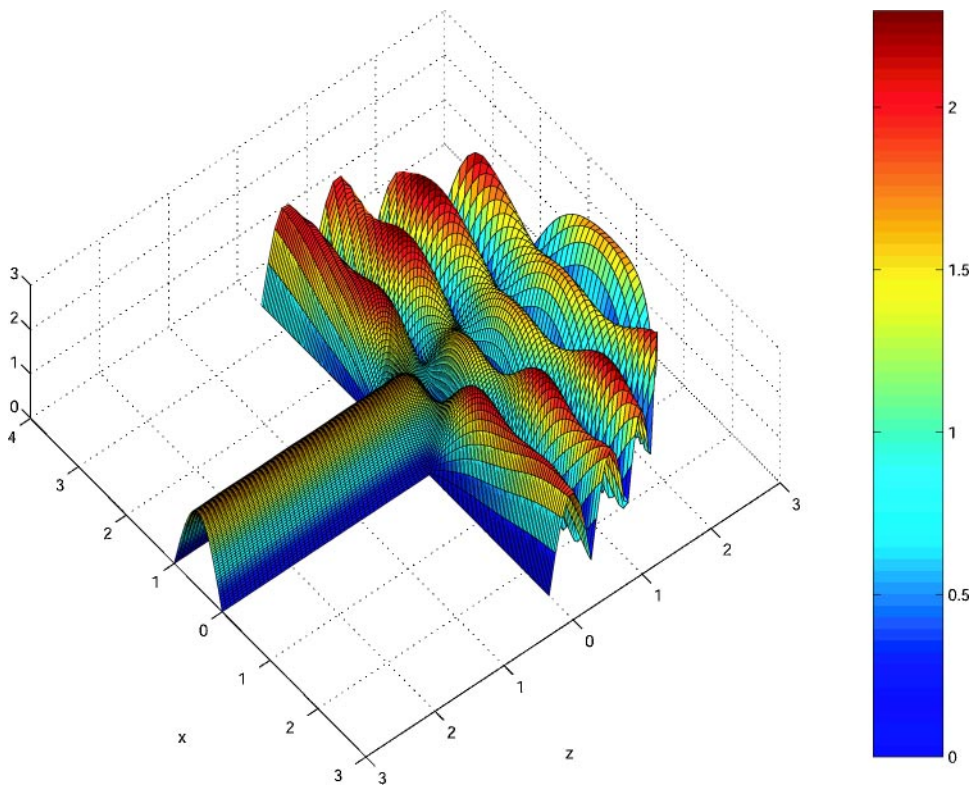

FIG. 12. Electric field amplitude $|W|$ for the receiving antenna problem (OHG grid) when $r_\infty = 3$, $z_\infty = 3$, $N_1 = 100$, $N_2 = 120$, and $N_g = 50$.

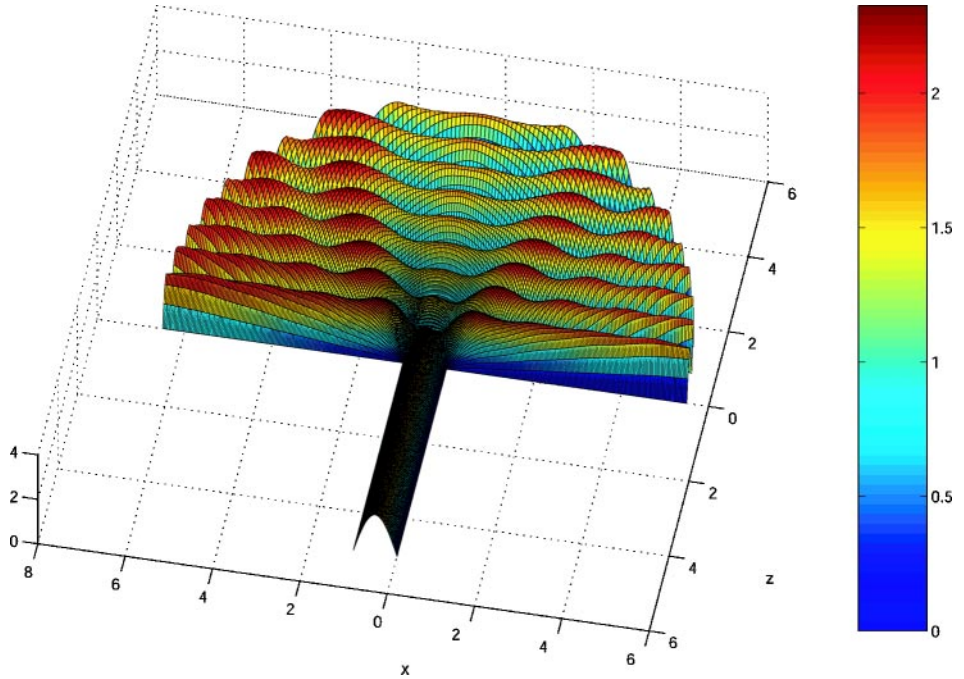

FIG. 13. Electric field amplitude $|W|$ for the receiving antenna problem (OHG grid) when $r_\infty = 6$, $z_\infty = 5$, $N_1 = 180$, $N_2 = 220$, and $N_g = 70$.

while in Fig. 13 $r_\infty = 6$ was used. The appropriate step sizes for these two cases were $\Delta t = 4 \times 10^{-4}$ and $\Delta t = 2 \times 10^{-4}$, respectively. These step sizes were experimentally determined to guarantee stability. Figures 12 and 13 reval the expected symmetric behavior and show a conic region in front of the aperture, where the total field is smaller compared with the rest of the domain. As a consequence, the scattered wave is larger in this conic region. Inside the waveguide, the incident plane wave is transformed into a single waveguide discrete mode of amplitude $|W| \approx 1.7$.

For comparison purposes maximum values of the amplitude $|W|$ of the total electric field are defined by regions. We designate

$Ml : |W_{i,j}|$ maximum for $i = 1, 2 \le j \le N_1 - 1$ (left boundary).
$Mg : |W_{i,j}|$ maximum for $2 \le i < N_g, 2 \le j \le N_1 - 1$ (guide inner region).
$Ma : |W_{i,j}|$ maximum for $i = N_g, 2 \le j \le N_1 - 1$ (aperture region).
$Mo : |W_{i,j}|$ maximum for $N_g < i < N_2, 2 \le j \le N_1 - 1$ (inside fan region).
$Mr : |W_{i,j}|$ maximum for $i = N_2, 2 \le j \le N_1 - 1$ (right boundary).

In Table VI, maximum values of the amplitude $|W|$ of the total electric field over TTM grids are compared for various grids refinement. In all these experiments the frequency k was held fixed as $k = 3\frac{\pi}{2}$. The parameters Iters represents the total number of iterations required for the time-dependent method to reach the time harmonic steady-state solution. From our experiments, we observe that the maximum values of the total electric field over a grid $N_1 \times N_2(N_g) = 70 \times 70(30)$ are very similar to those obtained over finer grids. However, as we will see later from the fan domain problem experiments, the two grids $N_1 \times N_2(N_g) = 100 \times 120(50)$ and $N_1 \times N_2(N_g)) = 130 \times 150(50)$ lead to important accuracy improvements.

TABLE VI
Maximum Values of Electric Field Amplitude over TTM Grids in the FWA Domain for Various Grid Refinements and Varying Size Domains

r_∞/z_∞	Δt	$N_1 \times N_2$ (N_g)	Ml	Mg	Ma	Mo	Mr	Iters
3/3	5×10^{-4}	70×70 (30)	1.701	1.731	1.717	2.307	2.232	120×10^3
3/3	4×10^{-4}	100×120 (50)	1.705	1.721	1.724	2.297	2.254	150×10^3
3/3	3×10^{-4}	130×150 (50)	1.709	1.720	1.718	2.299	2.244	160×10^3
6/5	2×10^{-4}	180×220 (70)	1.720	1.741	1.733	2.331	2.188	240×10^3

The calculation over OHG grids is performed by regions. More precisely, in the aperture region $N_g - 2 \leq \xi \leq N_g$ and $2 \leq \eta \leq N_1$ the finite-difference wave equation in curvilinear coordinates used is (12), while outside this region we used the equation corresponding to orthogonal grids ($\beta = 0$). The results for OHG grids are qualitatively the same and quantitatively very similar to those obtained for TTM grids. They are shown in Table VII.

It is interesting to analyze the receiving antenna problem when the incident plane wave is not normal to the waveguide aperture. In the fi

TABLE VIII
Maximum Values of Electric Field Amplitude over TTM and OHG Grids in FWA Domain When the Incident Wave Angle Is Oblique and r_∞/z_∞ = 3/3

k	δ	Δt	$N_1 \times N_2$ (N_g)	Ml	Mg	Ma	Mo	Mr	Iters
$3\pi/2$	$\pi/4$	3×10^{-4}	130×150 (50)	0.905	1.07	1.121	2.336	2.016	160×10^3
$3\pi/2$	$\pi/4$	3×10^{-4}	130×150 (50)	0.886	1.091	1.142	2.360	2.033	150×10^3
8	$\pi/6$	5×10^{-5}	180×200 (90)	1.874	2	1.816	2.343	2.201	325×10^3

numerical solution depends on the type of grid. Equation (26) is used for TTM grids, while Eq. (12) with $\beta = 0$ is used for OG grids. Comparison with the exact solution allowed us to establish the accuracy of the method. The results for normal incidence ($\delta = 0^\circ$) and TTM grids are summarized in Table IX, and for OG grids in Table X. We call E and E_b the absolute errors in the inner region and the fictitious infinite boundary, respectively. More precisely,

$$E = \max_{2 \le j < N_1 - 1,\ 2 \le i \le N_2 - 1} \| W(z_{i,j}, x_{i,j}, t_\infty)| - |W_{i,j}\|,$$

$$E_b = \max_{i = N_2,\ 2 \le j \le N_1 - 1} \| W(z_{i,j}, x_{i,j}, t_\infty)| - |W_{i,j}\|.$$

It is observed from Tables IX and X that accuracy is about the same for both types of grids. Also, there is a slight but not a significant advantage in using OHG grids over TTM

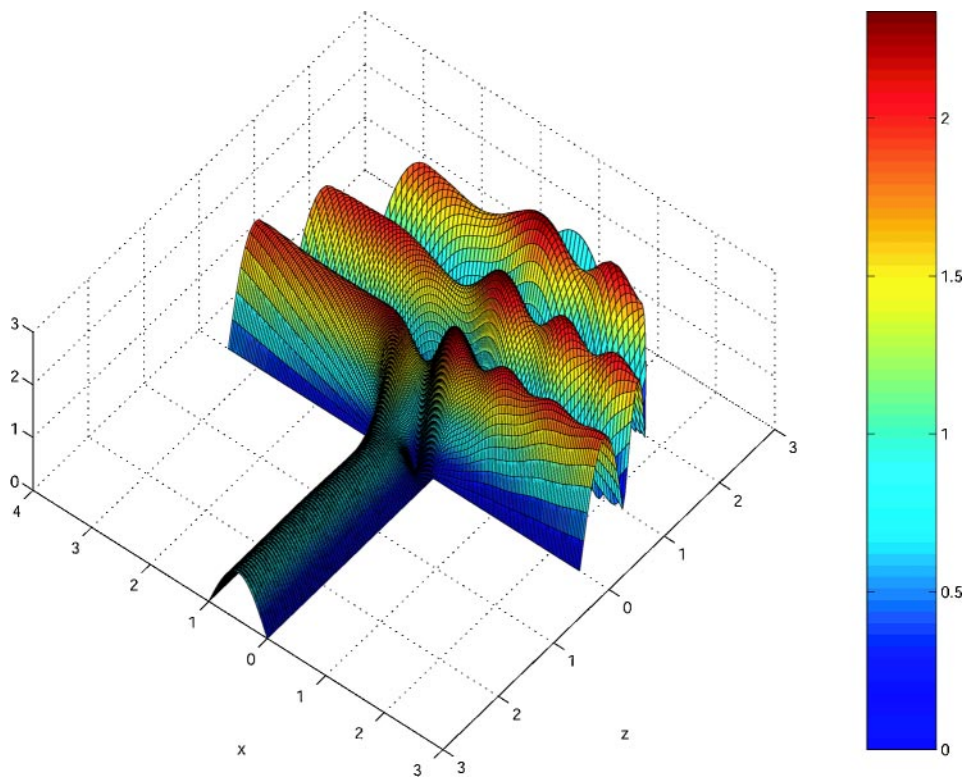

FIG. 14. Electric field amplitude $|W|$ for the receiving antenna problem when the incident wave angle $\delta = 45^\circ$ (OHG grid) and $r_\infty = 3$, $z_\infty = 3$, $N_1 = 130$, $N_2 = 150$, and $N_g = 50$.

TABLE IX
Numerical Experiments of Scattering from a PEC Wall for TTM Grids

r_∞	$N_1 \times N_2$	Δt	Mo	Mr	E	E_b	Iters
3	75×45	6×10^{-4}	2.05	2.06	0.13	0.15	24×10^3
3	100×60	4×10^{-4}	2.03	2.03	0.07	0.08	40×10^3
3	130×90	3×10^{-4}	2.008	2.02	0.03	0.04	70×10^3
3	180×120	9×10^{-5}	2.01	2.01	0.024	0.022	175×10^3
6	180×150	10^{-4}	2.02	2.07	0.089	0.104	128×10^3

TABLE X
Numerical Experiments on Scattering from a PEC Wall for OG Grids

r_∞	$N_1 \times N_2$	Δt	Mo	Mr	E	E_b	Iters
3	75×45	6×10^{-4}	2.07	2.08	0.145	0.159	22×10^3
3	100×60	4×10^{-4}	2.04	2.042	0.09	0.03	36×10^3
3	130×90	3×10^{-4}	2.014	2.025	0.035	0.052	60×10^3
6	180×150	10^{-4}	2.026	2.068	0.075	0.109	115×10^3

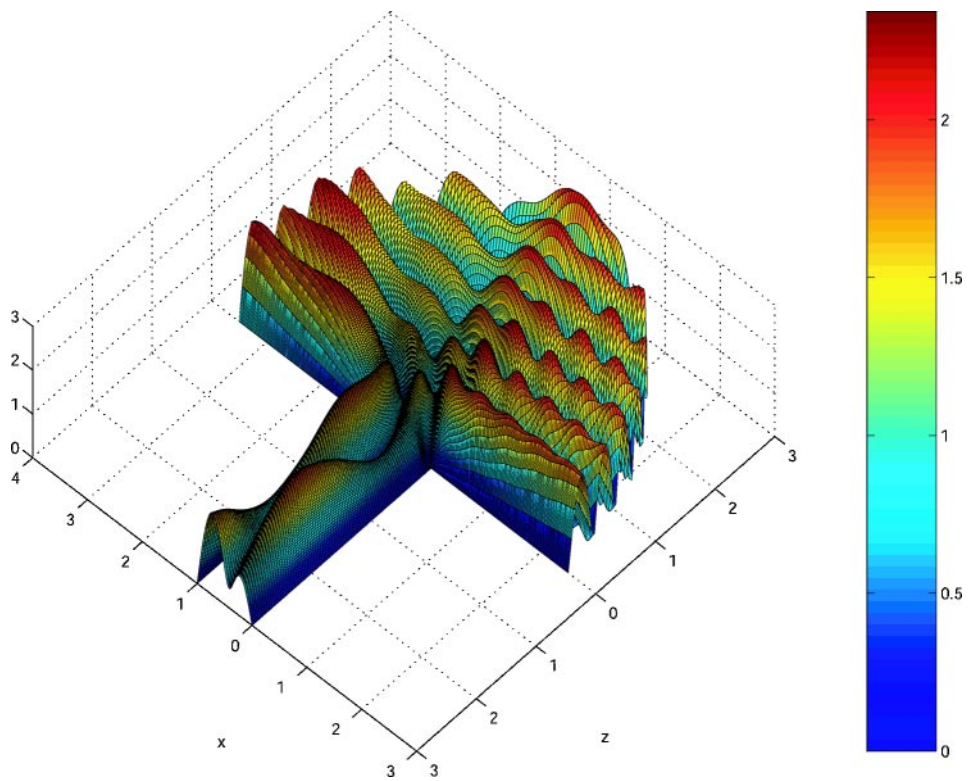

FIG. 15. Electric field amplitude $|W|$ for the receiving antenna problem when the incident wave angle $\delta = 30^\circ$ (TTM grid) and $r_\infty = 3$, $z_\infty = 3$, $N_1 = 180$, $N_2 = 200$, $N_g = 90$, and $k = 8$.

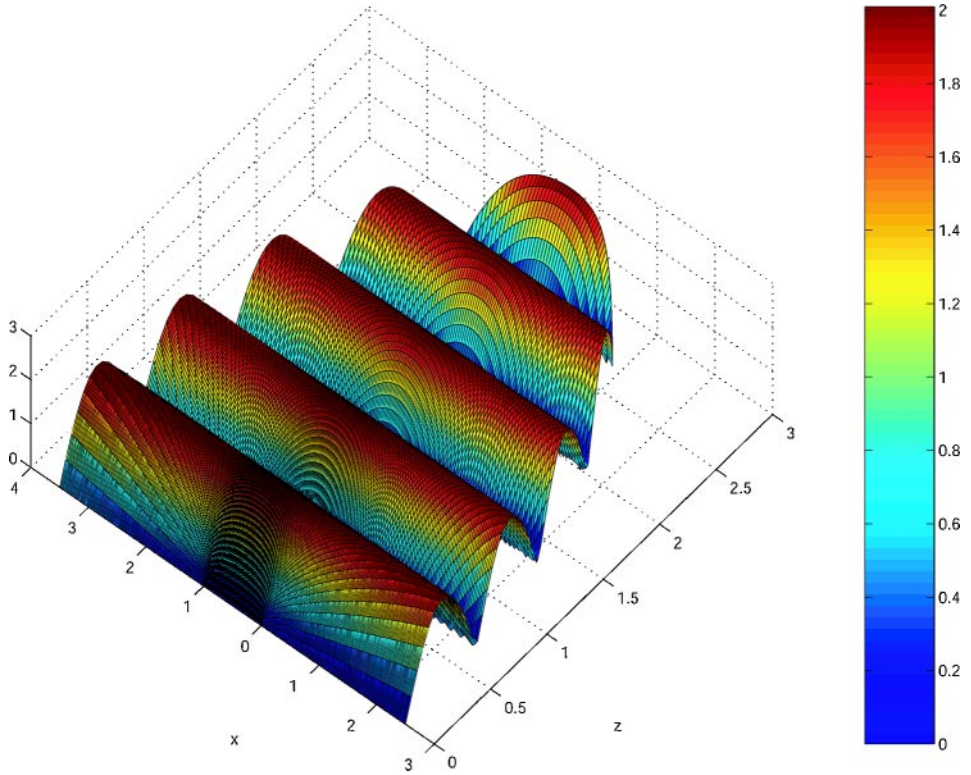

FIG. 16. Electric field amplitude $|W|$ for the scattering from a PEC wall (TTM grid) when $r_\infty = 3$, $N_1 = 180$, and $N_2 = 120$.

grids in terms of the number of iterations required to reach the steady state. In Fig. 16, the wave pattern is shown. The data used to obtain this figure are recorded in the fourth row of Table IX. We chose several coordinate lines to compare evaluation of the exact and approximate solutions over them. These results are presented in Figs. 17–19 for a 180×120 TTM grid. Excellent agreement was found for this grid size. A grid that fine was required to achieve the accuracy obtained in these experiments. More precisely using the energy norm to measure the error on these coordinate lines, we obtained the following results:

$$E_{2,\Delta z_{z\approx 1/2}} = \|W(z_{i,j}, x_{i,j}, t_\infty)| - |W_{i,j}\|\Delta z_i = 1.46 \times 10^{-2}, \tag{28}$$

$$E_{2,\Delta\theta_{r=r_{infty}}} = \|W(z_{i,j}, x_{i,j}, t_\infty)| - |W_{i,j}\|\Delta\theta_k = 1.83 \times 10^{-2}, \tag{29}$$

$$E_{2,\Delta\theta_{i=40}}(\text{interm. arc}) = \|W(z_{i,j}, x_{i,j}, t_\infty)| - |W_{i,j}\|\Delta\theta_k = \ 5.9 \times 10^{-3}. \tag{30}$$

5. APPLICATION OF THE TD-BCC METHOD TO HORN ANTENNAS

In this section, the method is applied to horn antennas with more realistic flare angles. We study the scattering from a horn antenna with a 60° flare angle and a smooth bend at the aperture. This antenna will be called a curved horn antenna (CHA). We also analyze the scattering from a horn antenna with a 60° flare angle and a nonsmooth bend at the aperture, which will be called a bent horn antenna (BHA). They are shown in Fig. 1. The curved horn antenna

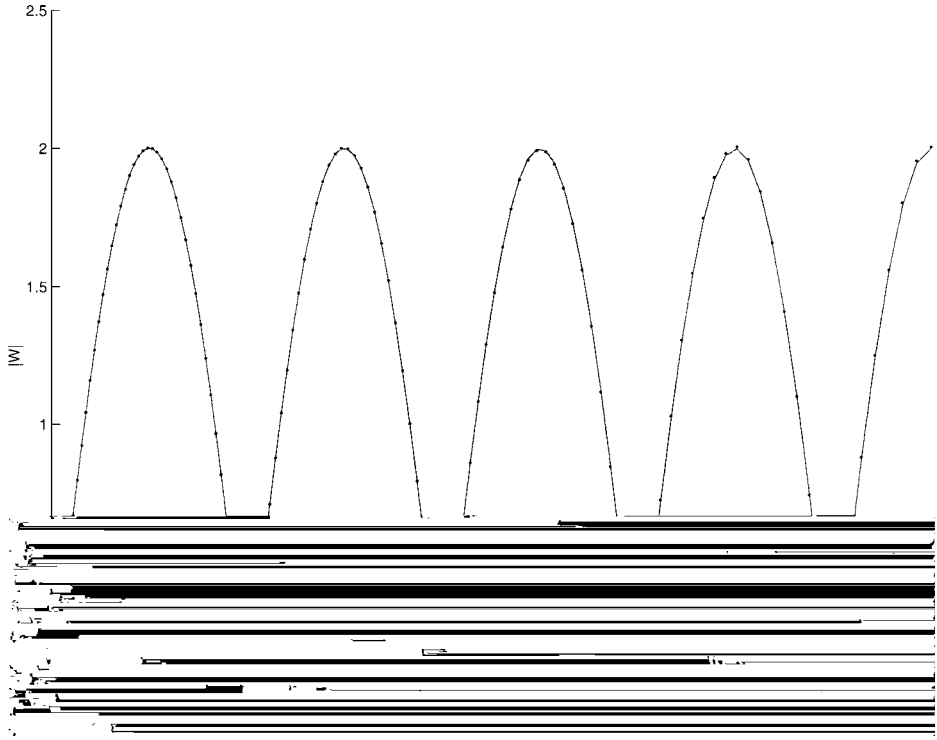

FIG. 17. Comparison of electric field amplitude $|W|$ for the scattering from a PEC wall along ray $j = 90$ when $r_\infty = 3$, $N_1 = 180$, and $N_2 = 120$. Solid line: exact solution; dotted line: TD-BCC approximate solution.

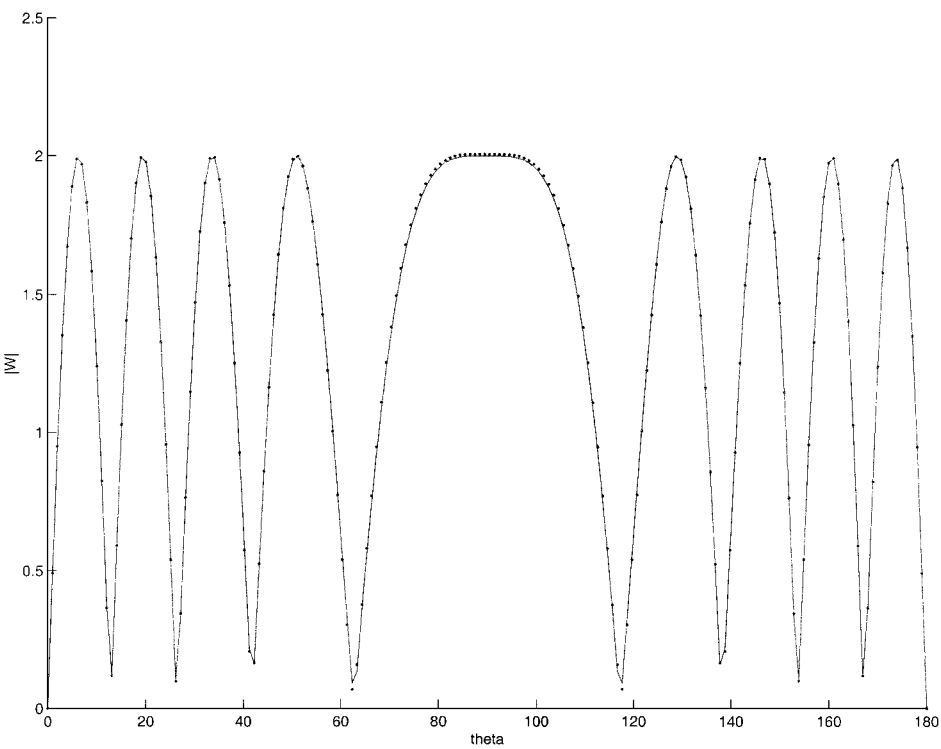

FIG. 18. Same as Fig. 17 except that solutions are shown along arc $i = 40$.

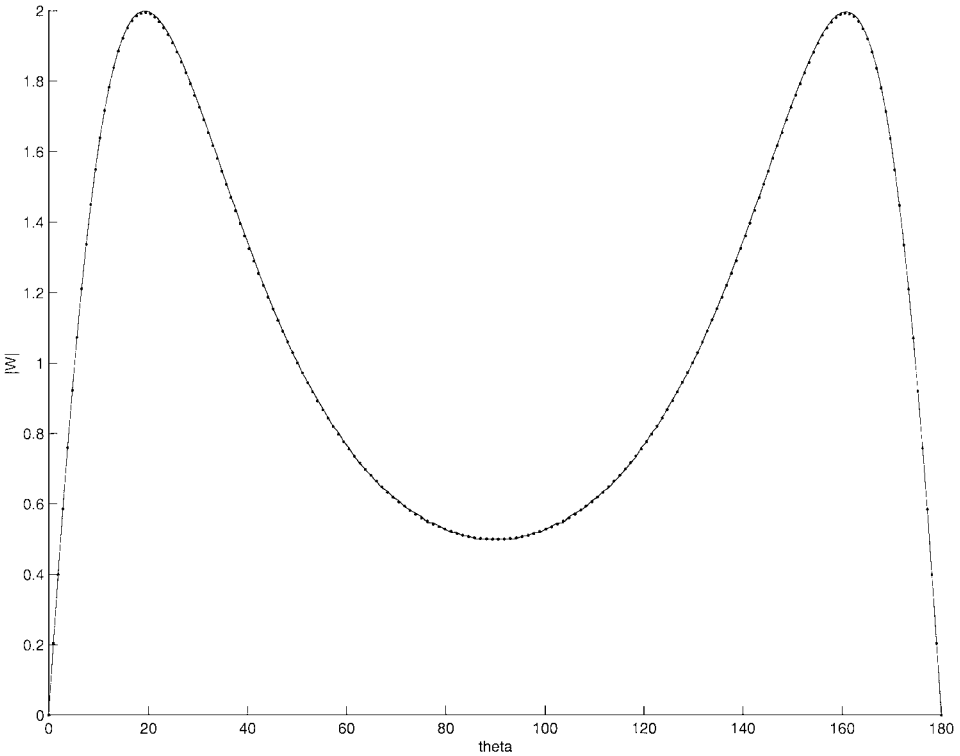

FIG. 19. Same as Fig. 17 except that solutions are shown along the fictitious infinite boundary $r_\infty = 3$.

was constructed by replacing the sharp corner at the aperture of the bent horn antenna by a second-degree Hermite polynomial, $p(z) = 1 + (\sqrt{3}/4L)(Z + L)^2$, $-L < z < L$. This polynomial matches the waveguide wall to the left at $z = -L$, and the oblique antenna wall to the right at $z = L$, smoothly. For purposes of comparison, the CHA was constructed identically to the BHA except in a small interval around the aperture. At this interval, the curved horn antenna was defined using the polynomial $p(z)$ with a moderate L value($L = 0.4$).

The scaled-Laplacian orthogonal algorithm performed well for this domain and relatively fine grids were obtained. Therefore, contrary to what we found for the FWA antenna, the almost orthogonal Hermite grid (OHG) algorithm was not needed for the horn antennas with 60° flare angle. In Fig. 20 TTM and almost orthogonal grids are shown. These graphs correspond to $50 \times 50\,(20)$ grids that were obtained for a tolerance of 10^{-4}. Results for different grid sizes are summarized in Table XI for the case of TTM grids, and Table XII contains results for OG grids. All these grids were obtained for a global tolerance of 10^{-4}. From Table XI, it is evident that the TTM algorithm converges faster for the CHA than for the BHA. Also, the maximum deviation from orthogonality is less severe for the CHA.

Concentration of grid lines at the aperture near the walls is observed for both types of antennas as shown in Fig. 20. As expected, the BHA experienced larger distortion at those aperture corner points than did the curved horn antenna. But surprisingly, the OG algorithm converges a little faster for the BHA than for the CHA when $r_\infty = 3$. Deviation from orthogonality is very similar for both cases as recorded in Table XII.

Electric field amplitude is shown in Fig. 21 for the BHA and in Fig. 22 for the CHA. These electric fields were obtained for a domain with $r_\infty = 6$ and $z_\infty = 5$ and grid size

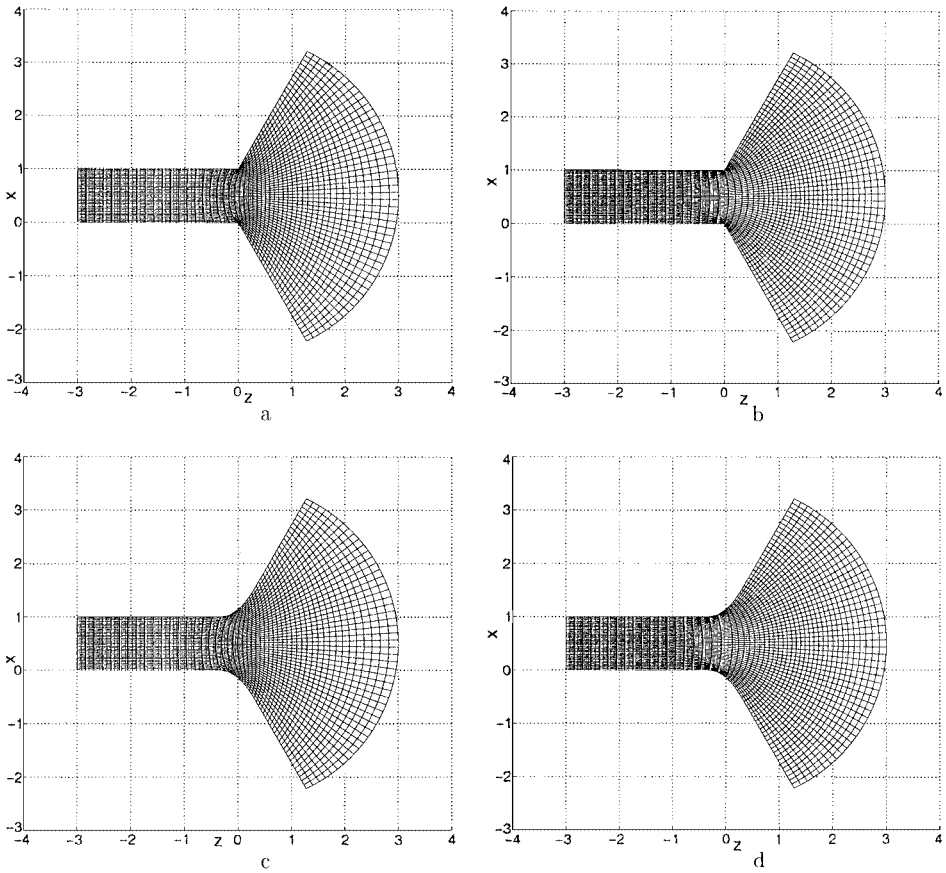

FIG. 20. TTM and OG grids for the horn antennas.

$180 \times 220\,(90)$. The time step required for stability was $\Delta t = 2 \times 10^{-4}$ in both cases. The wave pattern is very similar for both fields and very different from FWA. A comparison along an arc (arc number 110) is presented in Fig. 23. At this close distance from the aperture a slight difference is observed. The amplitude is higher for the CHA near the walls, but toward the middle, the BHA amplitude reaches a higher value than the CHA.

TABLE XI
TTM Grid Experiments for Horn Antennas

r_∞/z_∞	$N_1 \times N_2$ (N_g)	$J_{\min}$	MDO; (z, x)	ADO	Iters
		Bent horn antenna			
3/3	$50 \times 50\,(20)$	1.2×10^{-3}	65.5; $(-0.02, 0.02)$	9.7	114
3/3	$130 \times 150\,(50)$	1.2×10^{-4}	79.4; $(0.02, 1)$	11.3	502
6/5	$180 \times 220\,(90)$	7.8×10^{-5}	74.9; $(-0.02, 0)$	9.7	1266
		Curved horn antenna			
3/3	$50 \times 50\,(20)$	1.8×10^{-3}	64.8; $(-0.03, -0.1)$	9.7	113
3/3	$130 \times 150\,(50)$	1.8×10^{-4}	75.4; $(-0.03, -0.1)$	11.3	496
6/5	$180 \times 20\,(90)$	2.2×10^{-4}	68.7; $(-0.01, -0.2)$	9.8	942

TABLE XII
OG Grid Experiments for Horn Antennas

r_∞/z_∞	$N_1 \times N_2$ (N_g)	$J_{\min}$	MDO; (z, x)	ADO	*GIIts/InIts*
		Bent horn antenna			
3/3	50×50 (20)	2.1×10^{-4}	0.9; (0.06, −0.06)	0.03	38/574
3/3	130×150 (50)	6.7×10^{-6}	5.7; (0, 0)	0.4	30/1318
6/5	180×220 (90)	3.2×10^{-6}	2.1; (0, 0)	0.3	24/2388
		Curved horn antenna			
3/3	50×50 (20)	1.1×10^{-3}	0.5; (0.06, −0.2)	0.04	68/681
3/3	130×150 (50)	8.6×10^{-5}	3.6; (0, −0.2)	0.23	62/1447
6/5	180×220 (90)	1.5×10^{-4}	3.5; (0, −0.2)	0.3	24/2329

Thus, the smoothness of the antenna boundary at the aperture is responsible for a higher electric field amplitude near the walls. Table XIII contains electric field amplitude results for TTM and OG grids on both horn antennas. The effect of the 60° flare angle is not only seen in the new wave pattern compared with the FWA antenna, but also in the higher values of the electric field outside the waveguide. The convergence rate for the TD-BCC method is very similar for horn and flanged waveguide antennas as can be observed from Table XIII.

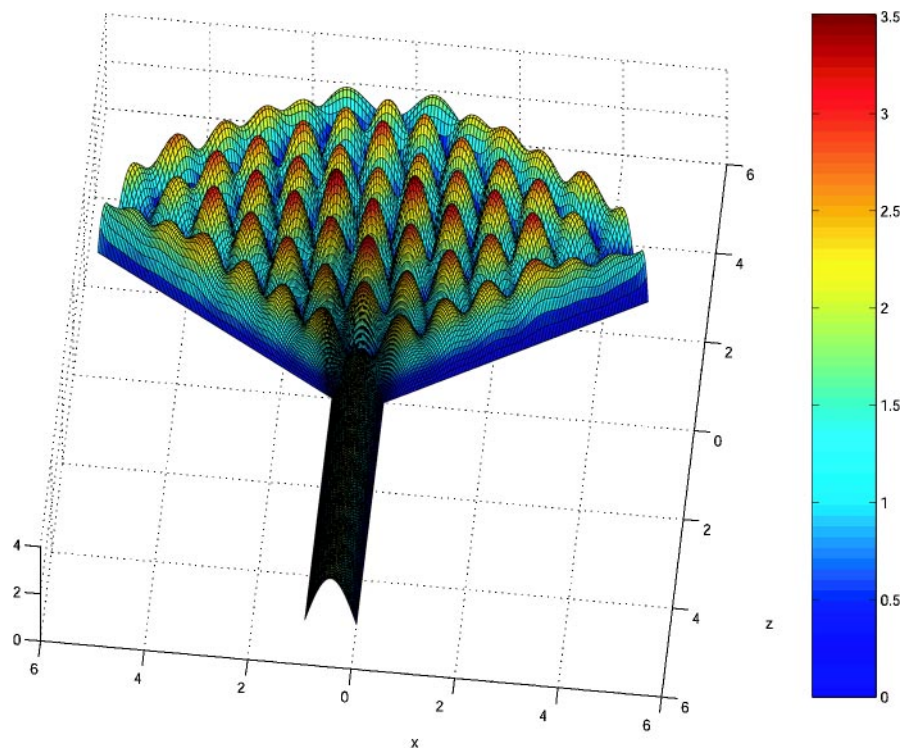

FIG. 21. Electric field amplitude $|W|$ for the receiving horn BHA problem when the incident wave angle $\delta = 0°$ (OG grid) and $r_\infty = 6$, $z_\infty = 5$, $N_1 = 180$, $N_2 = 220$, $N_g = 90$, and $k = 3\pi/2$.

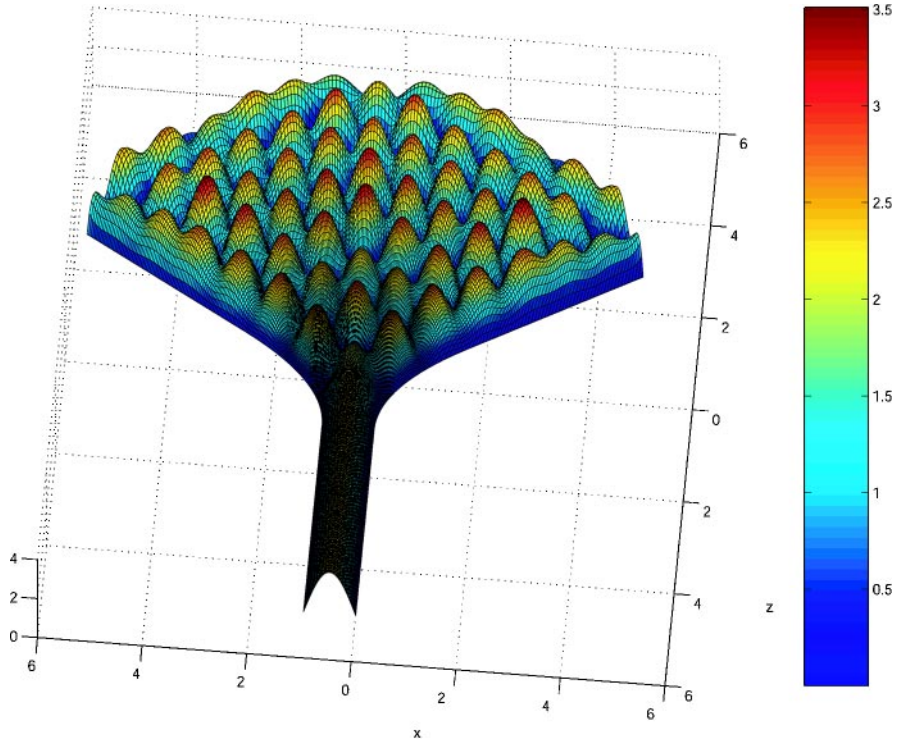

FIG. 22. Electric field amplitude $|W|$ for the receiving horn CHA problem when the incident wave angle $\delta = 0^\circ$ (OG grid) and $r_\infty = 6$, $z_\infty = 5$, $N_1 = 180$, $N_2 = 220$, $N_g = 90$, and $k = 3\pi/2$.

6. OPTICAL THEOREM FOR A FLANGED WAVEGUIDE ANTENNA WITH PERFECT ELECTRICAL CONDUCTOR WALLS

As pointed out in Section 3 the scattering problem described by wave equation (2) can also be modeled by the Helmholtz equation,

$$\nabla^2 V + k^2 V = 0, \quad \text{where } W(z, x, t_\infty) = V(z, x) e^{-ikt_\infty}. \tag{31}$$

In Section 2, we decomposed $W = W_{inc} + W_r + W_{sc}$, when $z > 0$ and $r = \sqrt{(x - 1/2)^2 + z^2} \to \infty$. Also, infinite boundaries were replaced by finite artificial boundaries at $z = z_\infty$ and $r = r_\infty$. Therefore, V can also be decomposed as $V = V_{inc} + V_r + V_{sc}$, when $z > 0$ and $r = r_\infty$, where $V_{inc} = e^{ik(-z\cos\delta + x\sin\delta)}$, $V_r = -e^{ik(z\cos\delta + x\sin\delta)}$, and $V_{sc} = A_0(\theta, \delta)\frac{e^{ikr}}{\sqrt{r}} + O(\frac{1}{r^{3/2}})$, when $r = r_\infty$. Therefore, the harmonic steady-state far field

TABLE XIII
Maximum Values of Electric Field Amplitude for Horn Antennas over TTM and OG Grids

Antenna/grid	$N_1 \times N_2$ (Ng)	Ml	Mg	Ma	Mo	Mr	Iters
BHA/TTM	180×220 (90)	1.85	1.9	1.88	3.52	2.2	255×10^3
CHA/TTM	180×220 (90)	1.95	2.01	1.95	3.50	2.22	245×10^3
CHA/OG	180×220 (90)	1.95	2.01	1.95	3.51	2.22	235×10^3

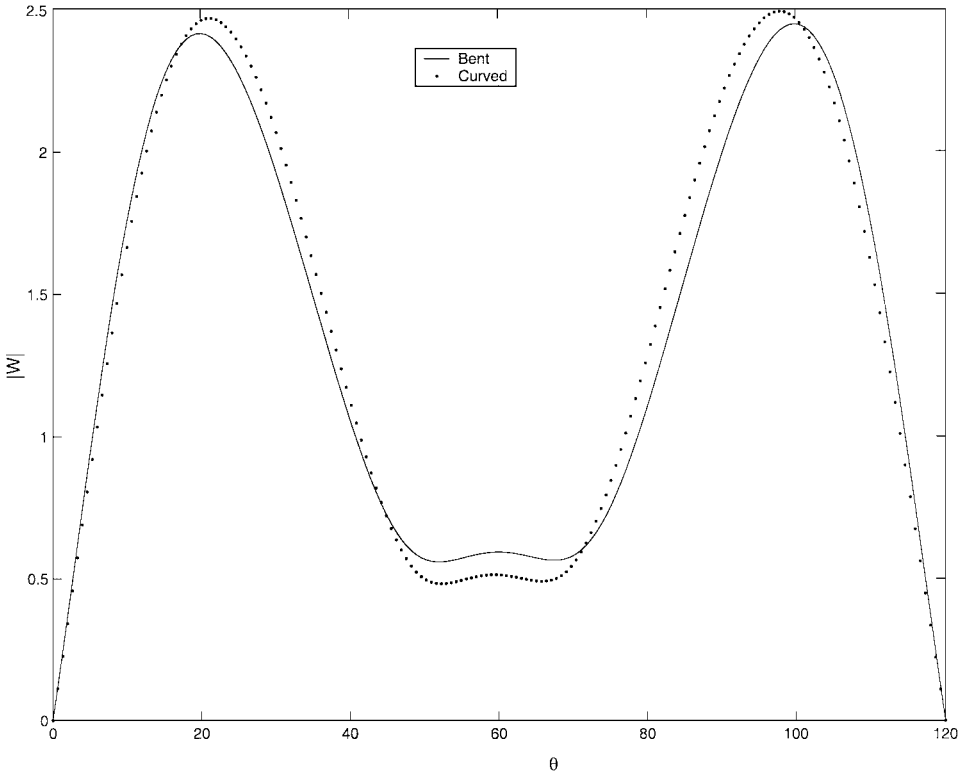

FIG. 23. Comparison of electric field amplitude $|W|$ for the scattering from a BHA and CHA along arc = 110, $r_\infty = 6$, $z_\infty = 5$, $N_1 = 180$, $N_2 = 220$, $N_g = 90$, and $k = 3\pi/2$.

amplitude is given by

$$V(r_\infty, \theta) = -2i \sin(kz \cos\delta) e^{ikx \sin\delta} + A_0(\theta, \delta) \frac{e^{ikr_\infty}}{\sqrt{r_\infty}} + O\left(\frac{1}{r_\infty^{3/2}}\right), \tag{32}$$

where $x = \frac{1}{2} + r_\infty \sin\theta$ and $z = r_\infty \cos\theta$.

On the other hand, the steady field inside the waveguide can be represented as

$$V(z, x) = \sum_{n=1}^{\infty} T_n(\delta) e^{-ik_n z} \sin(n\pi x), \quad z \le 0. \tag{33}$$

Following a recent derivation of an optical theorem for the sound hard flanged waveguide by Kriegsmann [24], an equivalent optical theorem,

$$k\Sigma_{r_\infty} + \frac{1}{2} \sum_{n=1}^{M} k_n |T_n|^2 = \sqrt{8\pi k}\, \mathrm{Re}\left[e^{i(\frac{\pi}{4} - \frac{k}{2}\sin(\delta))} A_0(\delta, \delta)\right], \tag{34}$$

for the flanged waveguide with PEC walls as shown in Fig. 2 can be derived. In Eq. (34),

$$\Sigma_{r_\infty} = \int_{-\pi/2}^{\pi/2} |A_0(\theta, \delta)|^2 \, d\theta \tag{35}$$

represents the total scattering cross section, and M is the largest integer for which the frequency k_n is real. A proof of (34) follows. First, it can be easily shown from Eq. (31) that $\mathrm{Im}[\nabla.(V^\star \nabla V)] = 0$, where $\star$ denotes the complex conjugate, and Im the imaginary part of a complex number. Integrating this expansion throughout the bounded region enclosed in Fig. 2, applying Green's theorem, and using boundary conditions yield

$$I_1 - I_2 = \mathrm{Im}\left[\int_{-\pi/2}^{\pi/2} V^\star \frac{\partial V}{\partial r}|_{r=r_\infty} r_\infty \, d\theta\right] - \mathrm{Im}\left[\int_0^1 V^\star \frac{\partial V}{\partial z}|_{z=z_\infty} \, dx\right] = 0. \tag{36}$$

Substitution of (33) into the expression corresponding to I_2 in (36) leads to

$$I_2 = \mathrm{Im}\left[-\frac{i}{2}\sum_{n=1}^{\infty} k_n\right.$$

Finally, substituting the above expressions for J_2 and J_3 in (42) and subtracting I_2 from I_1 lead to (34). The extra factor $e^{-ik/2\sin\delta}$, which is not present in the sound hard optical theorem [24], results from the difference in coordinate origin location.

In [24], it is stated that any approximate solution of a given numerical method for our antenna BVP needs to preserve the conservation law of the original problem. We now proceed to verify that our approximate solutions obtained by application of TD-BCC satisfy the optical theorem, Eq. (34).

First, we need to compute the scattered far field amplitude $A_0(\theta, \delta)$ from the numerical solution of the total electric field $W(r_\infty, \theta, t_\infty)$. From Eqs. (31) and (32), $A_0(\theta, \delta)$ can be approximated as

$$A_0(\theta, \delta) = \sqrt{r_\infty} e^{-ikr_\infty} \left[W(r_\infty, \theta, t_\infty) e^{ikt_\infty} + 2i \sin(kz \cos\delta) e^{ikx \sin\delta} \right]. \tag{43}$$

The scattering cross section, Σ_{r_∞} is obtained by numerical integration along the interval $[-\pi/2, \pi/2]$ after substitution of (43) into the expression (35) of the scattering cross section.

Transmission coefficients for the solution inside the waveguide, T_1 and T_2, can also be computed from the total electric field. In fact, from (31) and (33) we can solve for T_1 and evaluate at $x = 1/2$ to obtain

$$T_1 = W(z_\infty, 1/2, t_\infty) e^{ik_1 z_\infty} e^{ikt_\infty} + T_3 e^{-ik_3 z_\infty} e^{ik_1 z_\infty} + O\left(e^{|k_5| z_\infty}\right). \tag{44}$$

The term corresponding to T_3, although small, may be important to the computation of T_1 by (44). T_3 can be computed by applying the annihilating operator D_1, obtained from $D_n = \frac{\partial}{\partial z} + ik_n$, for $n = 1$, to the total steady field V in terms of the total field W. If solving for T_3 and evaluating at $x = 1/2$ and $z = z_\infty$, then

$$T_3 = \frac{i e^{ik_3 z_\infty} e^{ikt_\infty}}{k_1 - k_3} D_1 W(z_\infty, 1/2, t_\infty) + O\left(e^{|k_5| z_\infty}\right). \tag{45}$$

Error terms in the above expressions are exponentially small, since $z_\infty < 0$. When frequency $k \leq 2\pi$, there is only one mode propagating inside the guide. However, if this frequency is raised over 2π, there are more modes. For instance, experiments for $k = 8$ give two modes inside the guide when the incident angle is $\delta = \pi/6$, as shown in Fig. 15. The expression for T_2 is computed by solving for T_2 in (33), evaluating at $x = 1/4$, and keeping the term corresponding to coefficient T_3. In fact,

$$\begin{aligned} T_2 = e^{ik_2 z_\infty} \big[& W(z_\infty, 1/4, t_\infty) e^{ikt_\infty} - T_1 e^{-ik_1 z_\infty} \sin(\pi/4) \\ & - T_3 e^{-ik_3 z_\infty} \sin(3\pi/4) \big] + O(e^{|k_5| z_\infty}). \end{aligned} \tag{46}$$

We ran several experiments over almost orthogonal grids varying frequency k, incident angle δ, grid size $N_1 \times N_2$, and domain size r_∞ / z_∞. In Table XIV, we have recorded the results. The last column corresponds to the result obtained by dividing the right-hand side by the left-hand side in Eq. (34) for each experiment. This shows that our approximate solutions obtained by application of the time-dependent numerical methods with boundary-conforming curvilinear coordinates satisfy very closely the optical theorem, Eq. (34).

TABLE XIV
Validation of Numerical Solutions against Optical Theorem, Eq. (34)

k	δ	$N_1 \times N_2$	r_∞/z_∞	Sides ratio
$3\pi/2$	0	100×120	3/3	1.03
$3\pi/2$	0	181×200	3/3	0.999
$3\pi/2$	0	180×220	6/5	1.05
$3\pi/2$	$\pi/4$	130×150	3/3	1.01
8	0	180×200	3/3	1.02
8	$\pi/6$	180×200	3/3	1.004

7. SUMMARY AND CONCLUDING REMARKS

In this article an unstaggered finite-difference time-dependent algorithm based on numerically generated global curvilinear coordinates has been proposed to accurately model scattering from prototypical antennas in 2D. An attractive feature of this work is the study of the influence of non-cartesian orthogonal grids in the accuracy of the numerical approximation for the electric field. To the best of our knowledge this is the first time that globally orthogonal grids other than cartesian grids have been used to numerically model scattering of electromagnetic waves from arbitrarily shaped domains. Three types of grid generation algorithms based on numerical solutions of elliptic PDEs are compared. The popular nonorthogonal TTM algorithm used in many fluid dynamic problems, the scaled-Laplacian algorithm, which produces almost orthogonal grids (OG algorithm), and a new hybrid method that combines OG algorithm with Hermite interpolation (OHG algorithm). The advantage of this approach is that it only requires a parametric description of the boundaries and definition of boundary conditions over them. Therefore, the bookkeeping usually involved with other locally conforming methods is avoided.

The TD-BCC method achieved a reasonable accuracy for approximations of the electric field over grids with more than 100×100 nodes as shown in Tables IX and X. The OG algorithm failed to generate grids finer than 70×70 due to an undesirable concentration of grid lines at the aperture of the flanged waveguide domain as shown in Fig. 8. To overcome this problem, the OHG algorithm was devised in the present study. By means of OHG, it was possible to numerically generate sufficiently fine almost orthogonal grids for domains with abrupt changes up to 270° at corner points as those found in the flanged waveguide domain.

Another interesting feature of the present work is a derivation of an optical theorem for the flanged waveguide antenna with PEC walls. This theorem establishes a relationship among the scattering cross section, transmission coefficients of the solution inside the waveguide, and the leading-order term of the far field amplitude in the direction the incident wave. This theorem allows an independent validation of the numerical results obtained by any numerical technique. Our results were within 1–5% error according to this theorem (see Table XIV). No spurious reflections were observed after fictitious infinite boundaries were placed 3 to 6 units apart from the origin, where appropriate local annihilating operators were defined. As a result, our computations were free of late time instability observed in other nonorthogonal FDTD algorithms. Through numerical experimentation, it was determined that a time step from 5×10^{-4} to 2×10^{-4} was needed for numerical stability purposes when grids over 100×100 and upto 180×220 nodes were used for moderate frequencies

$ka = 3\pi/2$, 8 (see Tables VI–X and XIII). Horn antennas with a 60° flare angle and with sharp (BHA) and smooth (CHA) corners at the aperture were studied. A higher electric field amplitude was obtained near the walls for the CHA. The TD-BCC convergence results over the different grids revealed a slight advantage when OG and OHG grids were used. We believe that the use of non-cartesian almost orthogonal grids may be even more advantageous in scattering problems from arbitrary obstacles with interfaces and Neumann type boundary conditions.

ACKNOWLEDGMENTS

The authors thank Dr. G. A. Kriegsmann for several helpful discussions and for the provision of facilities at the New Jersey Institute of Technology during the early stage of the present work. They also thank Dr. Eliezer Correa for providing computer resources at CIOMMA Universidad Central de Venezuela and Luvic Figuera for helping with some of the grid generation computations. Finally, the insightful and constructive comments of the anonymous reviewers are greatly appreciated.

REFERENCES

1. A. Bayliss and E. Turkel, Radiation boundary conditions for wave-like equations, *Comm. Pure Appl. Math.* **33**, 707 (1980).
2. A. Bayliss and E. Turkel, Boundary conditions for the numerical solution of elliptic equations in exterior regions, *SIAM J. Appl. Math.* **42**, 430 (1982).
3. J. J. Bowman, T. B. Senior, and P. L. Uslengui, *Electromagnetic and Acoustic Scattering by Simple Shapes* (North-Holland, Amsterdam, 1969).
4. A. C. Cangellaris and D. B. Wright, Analysis of the numerical error caused by the stair-stepped approximation of a conducting boundary in FDTD simulations of electromagnetic phenomena, *IEEE Trans. Antennas Propagat.* **39**, 1518 (1991).
5. S. Dey and R. Mittra, A locally conformal finite-difference time-domain (FDTD) algorithm for modeling three-dimensional perfectly conducting objects, *IEEE Microwave Guided Wave Lett.* **7**, 273 (1997).
6. S. Dey, R. Mittra, and S. Chebolu, A technique for implementing the FDTD algorithm on a nonorthogonal grid, *Microwave Opt. Technol. Lett.* **14**, 213 (1997).
7. L. Eca, 2D orthogonal grid generation with boundary point distribution control, *J. Comput. Phys.* **125**, 440 (1996).
8. M. Fusco, FDTD algorithm in curvilinear coordinates, *IEEE Trans. Antennas Propagat.* **38**, 78 (1990).
9. M. Fusco, M. Smith, and L. Gordon. A three-dimensional FDTD algorithm in curvilinear coordinates, *IEEE Trans. Antennas Propagat.* **39**, 1463 (1991).
10. S. Gedney, F. Lansing, and D. Rascoe, A generalized Yee-algorithm for the analysis of MMIC devices, *IEEE Trans. Microwave Theory Tech.* **44**, 1393 (1996).
11. S. Gedney and J. Roden, Numerical stability of nonorthogonal FDTD methods. *IEEE Trans. Antennas Propagat.* **48**, 231 (2000).
12. R. Haberman, *Elementary Applied Partial Differential Equations* (Prentice Hall, New York, 1998).
13. T. Hagstrom and S. I. Hariharan, A formulation of asymptotic and exact boundary conditions using local operators, *Appl. Numer. Math.* **5**, 1 (1998).
14. Y. Hao and C. J. Railton, Analyzing electromagnetic structures with curved boundaries on Cartesian FDTD meshes, *IEEE Trans. Microwave Theory Tech.* **46**, 82 (1998).
15. R. Holland, Finite-difference solution of Maxwell's equations in generalized nonorthogonal coordinates, *IEEE Trans. Nucl. Sci.* **NS-30**, 4589 (1983).
16. R. Holland, Pitfalls of staircase meshing, *IEEE Trans. Electromag. Compat.* **35**, 434 (1993).
17. R. Janaswamy and Y. Liu, An unstaggered colocated finite-difference scheme for solving time-domain Maxwell's equations in curvilinear coordinates, *IEEE Trans. Antennas Propagat.* **45**, 1584 (1997).

18. R. Jimenez, *Solución Numérica de un Problema de Dispersión de Ondas Acústicas con Aplicación del Principío de Amplitud Límite*, Master's thesis (Fac. de Ciencias, Universidad Central de Venezuela, 1995).
19. T. G. Jurgens, A. Taflove, K. Umashankar, and T. G. Moore, Finite-difference time-domain modeling of curved surfaces, *IEEE Trans. Antennas Propagat.* **41**, 357 (1992).
20. D. Katz, M. Piket-May, A. Taflove, and K. Umashankar, FDTD analysis of electromagnetic wave radiation from systems containing horn antennas, *IEEE Trans. Antennas Propagat.* **39**, 1203 (1991).
21. P. Knupp and S. Steinberg, *Fundamentals of Grid Generation* (CRC Press, Boca Raton, FL, 1993).
22. G. A. Kriegsmann, Exploiting the limiting amplitude principle to numerically solve scattering problems, *Wave Motion* **4**, 371 (1982).
23. G. A. Kriegsmann, Radiation conditions for wave guide problems, *SIAM J. Sci. Stat. Comput.* **3**, 318 (1982).
24. G. A. Kriegsmann, The flanged waveguide antenna: Discrete reciprocity and conservation, *Wave Motion* **29**, 81 (1999).
25. J.-F. Lee, Finite difference time domain algorithm for non-orthogonal grids and its application to the solution of electromagnetic scattering problems, *Arch. Elektron. Uebertragungstech.* **46**, 328 (1992).
26. C. Liao, Y. Den, and L. Jen, Solution for EM scattering about arbitrary two-dimensional bodies with the use of the Thompson–FDTD method, *Microwave Opt. Technol. Lett.* **13**, 233 (1996).
27. C. Liao, Y. Shao, and W. Lin, A new method for calculating electromagnetic scattering of complex objects, *Microwave Opt. Technol. Lett.* **9**, 144 (1995).
28. R. T. Ling, A time-dependent method for the numerical solution of wave equations in electromagnetic scattering problems, *Comput. Phys. Comm.* **68**, 213 (1991).
29. N. K. Madsen, Divergence preserving discrete surface integral methods for Maxwell's curl equations using non-orthogonal unstructured grids, *J. Comput. Phys.* **119**, 34 (1995).
30. P. Mezzanotte, L. Roselli, and R. Sorrentino, A simple way to model curved surfaces in FDTD algorithm avoiding staircase approximation, *IEEE Microwave Guided Wave Lett.* **5**, 267 (1995).
31. A. H. Mohammadian, V. Shankar, and W. F. Hall, Computation of electromagnetic scattering and radiation using a time-domain finite volume discretization procedure, *Comput. Phys. Comm.* **68**, 175 (1991).
32. C. S. Morawetz, The limiting amplitude principle, *Comm. Pure Appl. Math.* **15**, 349 (1962).
33. C. J. Railton and I. J. Craddock, Analysis of general 3-D PEC structures using improved CP-FDTD algorithm, *Electron. Lett.* **31**, 1553 (1995).
34. C. Reig, E. Navarro, and V. Such, FDTD analysis of E-sectoral horn antennas for broad-band applications, *IEEE Trans. Antennas Propagat.* **45**, 1484 (1997).
35. G. Ryskin and L. G. Leal, Orthogonal mapping, *J. Comput. Phys.* **50**, 71 (1983).
36. M. Sarmiento, *Principio de la Amplitude Límite Aplicado a Problemas de Dispersión con Generación de Mallas*, Master's thesis (Fac. de Ciencias, Universidad de los Andes, Mérida, Venezuela, 1996).
37. C. L. Scandrett, G. A. Kriegsmann, and J. D. Achenbach, Application of the limiting amplitude principle to elastodynamic scattering problems, *SIAM J. Sci. Stat. Comput.* **7**, 571 (1986).
38. J. B. Schneider and K. L. Shlager, FDTD simulations of TEM horns and the implications for staircased representations, *IEEE Trans. Antennas Propogat.* **45**, 1830 (1997).
39. V. Shankar, A. Mohammadian, and W. F. Hall, A time-domain finite-volume treatment for the Maxwell equations, *Electromagnetics* **10**, 127 (1990).
40. A. Taflove and M. E. Brodwin, Numerical solution of steady-state electromagnetic scattering problems using the time-dependent Maxwell's equations, *IEEE Trans. Microwave Theory Tech.* **23**, 623 (1975).
41. A. Taflove and S. C. Hagness, *Computational Electrodynamics. The Finite-Difference Time-Domain Method*, 2nd ed. (Artech House, Norwood, MA, 2000).
42. J. F. Thompson, F. C. Thames, and C. W. Mastin, Automatic numerical generation of body-fitted curvilinear coordinate system for field containing any number of arbitrary two-dimensional bodies, *J. Comput. Phys.* **15**, 299 (1974).

43. P. Tirkas and C. Balanis, Contour path FDTD method for analysis of pyramidal horns with composite innter *e*-plane walls, *IEEE Trans. Antennas Propagat.* **42**, 1476 (1994).
44. V. Villamizar and R. Jimenez, Scattering cross section of a cylinder at the interface of two acoustic media, *in Proc. 4th Int. Conf. Mathematical and Numerical Aspects of Wave Propagation Phenomena, Colorado, 1998*, edited by J. A. DeSanto (SIAM, Philadelphia, 1998), p. 641.
45. A. Winslow, Numerical solution of the quasilinear poisson equations in a nonuniform triangle mesh, *J. Comput. Phys.* **2**, 149 (1967).
46. K. S. Yee, Numerical solution of initial boundary value problems involving Maxwell's equations in isotropic media, *IEEE Trans. Antennas Propagat.* **14**, 302 (1966).